Turbulent Air Flow Measurement with the Aid of 3-D Particle Tracking Velocimetry in a Curved Square Bend.

Yuji Suzuki and Nobuhide Kasagi
Department of Mechanical Engineering, The University of Tokyo, Hongo, Bunkyo-ku, Tokyo 113-8656, Japan

January 26, 2000

Abstract. A three-dimensional particle tracking velocimeter (3-D PTV) was applied to air flow measurement in a strongly curved U-bend of a square cross-section. He-filled neutral-buoyant soap bubbles were employed as a flow tracer, and turbulent statistics including all Reynolds stress components were measured. The pressure-induced secondary flow, of which magnitude reached about 30% of the bulk mean velocity, was observed. The present experimental result is mostly in good agreement with the LDA data at higher bulk-mean Reynolds number taken by Chang et al. (1983). The effect of the secondary flow on the production mechanism of turbulent kinetic energy as well as on the distributions of the invariants of stress anisotropy tensor was examined in detail.

Keywords: curved duct, turbulent air flow, 3-D PTV, secondary flow

1. Introduction

Turbulent flow in conduits of complex geometry is often encountered in engineering equipment, such as fluid machinery and heat transfer devices. It is well known that the mean fluid motion perpendicular to the streamwise direction is generated in such conduits due to two different mechanisms, i.e., the secondary flows of Prandtl's first and second kinds. For instance, the secondary motion of Prandtl's first kind is caused by cross-stream pressure gradient in curved ducts, and its magnitude can be as large as 20–30% of the streamwise mean velocity. On the other hand, the secondary motion of Prandtl's second kind observed in non-circular ducts is caused by the inhomogeneity of the Reynolds stresses. The magnitude of this kind is very small, and of the order of 2–3% of the streamwise mean velocity. Since these secondary motions significantly affect heat and momentum transport processes, it is indespensible to understand the underlying physical mechanism and to develop a turbulence model that can predict them with reasonably high accuracy for various engineering applications.

In the last few decades, a number of investigations have been carried out both experimentally and numerically in order to examine the origin

of the secondary motion (e.g., Perkins, 1970; Melling and Whitelaw, 1976; Humphrey et al., 1981; Taylor et al., 1982; Demuren and Rodi, 1984; Choi et al., 1990; Sudo et al., 1998). Chang et al. (1983) employed laser-doppler anemometry (LDA, hereafter) to measure the development of a turbulent flow in a square-sectioned U-bend. They provided detailed experimental data and showed that the strong secondary flow produces a very complex three-dimensional flow structure, although the flow remains unseparated. The most notable feature of their experimental result is that there exist marked troughs in the streamwise velocity halfway around the bend. Iacovides et al. (1990) made a hot-wire anemometry (HWA, hereafter) measurement in a curved duct having the same bend geometry with a shortened inlet section, and reported that the effect of the inlet boundary layer thickness is minor. Azzola et al. (1986) found in their LDA measurement that the magnitude of secondary flow in a curved circular pipe is smaller than that in the corresponding curved square duct. Brundrett and Baines (1964) employed HWA and obtained all Reynolds stress tensor components in a turbulent straight square duct flow. Gavrilakis (1992) and Huser and Biringen (1993) separately made a direct numerical simulation (DNS, hereafter) of turbulent square duct flow, and obtained detailed turbulent statistics.

Recent development in digital image processing has enabled us to make field measurement of flow velocity (e.g., Adrian, 1991). Among various techniques, three-dimensional particle tracking velocimetry (3-D PTV, hereafter) has a great advantage of obtaining instantaneous vector distributions in a 3-D volume (Nishino et al., 1989; Kasagi and Nishino, 1992; Sata and Kasagi, 1992; Maas et al., 1993; Malik et al., 1993; Guezennec et al., 1994). It has already been successfully applied to various turbulent water flows (e.g., Nishino and Kasagi, 1989; Ninomiya and Kasagi, 1993; Suzuki and Kasagi, 1994; Sata and Kasagi, 1995; Kasagi and Matsunaga, 1995; Suzuki et al., 1999). However, only a few attempts have been made in air flows, although air flow measurement is of great importance in many engineering applications.

Sata et al. (1994) has developed a 3-D PTV system for air flow measurement, and applied it to the turbulent flow in a straight square duct. In the present study, their results are used to evaluate the performance of the present 3-D PTV system in air flow. A turbulent air flow in a square cross-sectioned curved duct is then measured, and the effect of streamline curvature on the turbulent statistics is investigated quantitatively. The production mechanism of turbulent kinetic energy and the distributions of invariants of the stress anisotropy tensor are also examined in detail.

2. 3-D particle tracking velocimetry (3-D PTV)

The 3-D PTV used in the present study was originally developed by Nishino and Kasagi (1989), Kasagi and Sata (1992) and Sata and Kasagi (1992) for liquid flow measurement, and modified by Sata et al. (1994) for air flow measurements. The technique is characterized by its use of three TV cameras that observe tracer particles suspended in a flow field from arbitrary viewing directions. Three velocity components are simultaneously measured by tracking each particle in a 3-D volume.

The present measurement system shown in Fig. 1 is composed of three CCD cameras, three laser disk recorders (Sony LVR-5000), a digital image processor (Nexus 6810, 512x480 pixels, 8bit gray level), three stroboscopes, and a timing signal generator. A series of TV frames taken by the cameras is consecutively recorded onto the laser disks. At the data reduction stage, replayed images are A/D converted by the image processor and then transferred to a workstation, where photographic coordinates and 3-D trajectories of the tracer particles are calculated. Details of camera calibration and particle tracking procedures can be found in Kasagi and Nishino (1992) and Sata and Kasagi (1992), respectively. Since the flow velocity is generally small in liquid flow experiments, a single stroboscope synchronized with the vertical drive (60 Hz) was employed in previous studies. A primary system modification by Sata et al. (1994) for air flow measurement is its use of multiple stroboscopes and the timing signal generator for reducing the time interval of the successive particle images.

Figure 2 shows the time sequence of image acquisition and illumination used in the present study schematically. One stroboscope is flashed before a vertical blanking period during the former TV field, while two stroboscopes are flashed during the latter field. Therefore, three successive instantaneous particle images at time intervals, Δt_1 and Δt_2, can be projected on two successive TV fields that compose one TV frame. The third pulses of the strobo light are employed in order increase the number of velocity vectors measured, since the number density of tracers in the present study is fairly low as described below. The time interval can be selected arbitrarily from 60 μs to 1/30 s and is chosen in such a way that the displacement of successive particle images becomes 20–50 pixels on the image plane.

3. Tracer particle

Tracer particles for turbulence measurement should have high frequency response to velocity fluctuations, and their diameter d should be smaller

than the turbulent micro scales (Kasagi and Nishino, 1992) if possible. Melling (1997) made an extensive review on tracer particles for both gas and liquid flows, and showed that various kinds of particles having several microns in diameter can be used for particle image velocimetry (PIV) measurement in air flows. However, particles having a much larger diameter are required for the present 3-D PTV system in order to obtain high accuracy in the photographic coordinates of the particle image (Nishino et al., 1989). Kato et al. (1992) and Adachi et al. (1993) employed plastic capsules ($d = 50\mu$m) as tracer particles. They obtained the turbulent statistics of a turbulent boundary layer and flow over a backward-facing step, both of which are in accordance with the previous studies.

Sata et al. (1994) examined two kinds of tracer particles; one is sphere plastic capsule (Expancel, Japan Ferrite Co., Ltd.) and the other is He-filled soap bubble (bubble, hereafter). Characteristics of these tracer particles are summarized in Table 1. The density of the plastic capsule is about 30 times larger than that of air. It is relatively easy to feed plastic capsules into a flow field and obtain high number density in the measurement volume. On the other hand, the bubble is almost neutrally buoyant, whilst its diameter is relatively large (0.5-1 mm) and the resultant number density is likely to remain small (Kent and Eaton, 1982).

Figure 3(a) shows a typical raw image of plastic capsules (Sata et al., 1994). Each particle is clearly seen, although many particles adhere to the wall due to static electricity as shown in the bottom part of the figure. Sata et al. (1994) concluded that spurious velocity vectors were significantly increased, since the images of particles adhered to the wall overlap those in the flow domain on the image plane. Figure 3(b) shows a typical image of bubbles. Each trajectory appears as six brightness points, which are actually three pairs of reflection points from the triple stroboscope flashes. Each pair of bright spots corresponds to the location where the incident light reflects on the inner and outer surface of the bubble (Oakley et al., 1997). The centroid of each bubble on the image plane is determined as the mid point of the neighboring two brightness peaks. Figure 4 shows the probability density of the distance between brightness peaks on particle images presently obtained. Since the most probable distance is around 9 pixels, pairs of brightness peaks located within 11 pixels are considered to be subject to a single bubble.

Mei (1996) proposes the equation of motion for particles, in which the drag force, the added-mass force, and the pressure-gradient force are considered, and derives the frequency response function of particles to periodic fluid motions. According to his formula, the relative amplitude

of particles η can be written as,

$$\eta = \sqrt{\frac{(1+\epsilon)^2 + (\epsilon + 2/3\epsilon^2)^2}{(1+\epsilon)^2 + \{\epsilon + 2/3\epsilon^2 + 4/9(\rho-1)\epsilon^2\}^2}}, \tag{1}$$

where $\rho(=\rho_p/\rho_f)$ is the density ratio of the particle and the fluid, and

$$\epsilon = \sqrt{\pi f d^2/(4\nu)}. \tag{2}$$

Figure 5(a) shows the frequency response of particles. Since the density of plastic capsules is very large, their traceability is decreased rapidly with increasing frequency. On the other hand, the bubble having almost neutral density shows a good frequency response; η at f <1kHz is more than 0.95 and 0.9 for bubbles having a density ratio of 1.1 and 1.2, respctively. Under the experimental condition in the curved duct described below, the Kolmogrov length and time scales are estimated to be about 130 μm and 900 Hz (1.1 ms), whereas the turbulent macro scales defined by the turbulent kinetic energy and the dissipation rate are about 12 mm and 60 Hz (17 ms), respectively. Sata et al. (1994) showed in their experiment that the traceability of both tracer particles is sufficient for the measurement of low-order turbulent statistics such as the mean and rms velocities, since most of the turbulent energy is included in turbulent motion of larger scales.

Figure 5(b) shows the radial terminal velocity of tracers due to the centrifugal force in a curved flow, where U, r and g are the streamwise velocity, the radius of the curved flow and the gravitational acceleration, respectively. The drag coefficient of the particle is assumed as

$$C_D = 24(1 + 0.15Re_p^{0.687})/Re_p, \tag{3}$$

where Re_p is the particle Reynolds number (Clift et al., 1978). In the present experimental condition, $U^2/(rg)$ is about 6, so that the radial velocity u_{rg} of bubbles (d=1mm) is less than 0.5 % of U when the density ratio is adjusted to be less than 1.1. On the other hand, u_{rg} of the plastic capsule ($d = 100\mu$m) is more than 1.5 % of U. A preliminary flow visualization showed that the plastic capsules ($d = 100\mu$m) were concentrated in the outer region of the bend. Although the plastic capsules having a diameter of 50μm have good traceability, but their image intensity would be too low for the strobo scopes presently employed.

Therefore, we have chosen bubbles as a flow tracer in the present study, since plastic capsules have two drawbacks, i.e., their adhesion to the wall and the large radial velocity induced in curved flows.

4. Experimental setup

Figure 6 shows a schematic of the curved air duct having a square cross-section. The hydraulic diameter H is 71 mm. The mean radius of the bend was chosen as $R_c = 3.35H$, which was the same as that of Chang et al. (1983). The test section was located 90 degrees downstream of the bend inlet, and the bottom half of the duct was measured by employing two measurement volumes covering the inner and outer regions of the bend. A glass plate was mounted on the top wall, and three CCD cameras were settled above the bend as shown in Fig. 7. Illumination was applied through the outer side wall of the bend, which was made of plexiglass. As shown in Fig. 7, the origin of the coordinate system was chosen at the center of the duct, and θ, r and z denote the tangential (streamwise), radial and vertical directions, respectively.

Figure 8 shows the locations of wall pressure taps. The static pressure was measured by using a precision pressure sensor. Figure 9 shows the distribution of the pressure coefficient C_p defined by

$$C_p = \frac{p - p_{ref}}{\rho U_m^2}, \tag{4}$$

where U_m denotes the bulk mean velocity, while the reference pressure p_{ref} was defined as the static pressure $8H$ upstream of the bend inlet. The dimensionless radial position r^* is defined as:

$$r^* = \frac{r - r_i}{r_o - r_i}, \tag{5}$$

where r_o and r_i denote the outer and inner radius, respectively. When the bulk Reynolds number $Re_m (= U_m H/\nu)$ =56200, C_p in the outer region is somewhat smaller than the data of Chang et al. (1983) for Re_m=56700, although the overall behavior is in good agreement with their result. For a lower Reynolds number of Re_m=17600, the distribution remains unchanged qualitatively, although the drop in C_p in the streamwise direction becomes larger as in a curved pipe (Ito, 1959).

Since the velocity vectors obtained by 3-D PTV were located randomly in the measurement volume, they were grouped into small data cells depending on their 3-D location. Then, the turbulent statistics were calculated as ensemble averages of velocity vectors in each cell. The dimension of the data cell the θ, r, and z directionsin were respectively $\Delta\theta$=1 degree, Δr=2 mm, Δz=2 mm.

According to ANSI/ASME PTC 19.1-1985, the uncertainties associated with the instantaneous velocities measured were estimated at 95 % coverage (Nishino et al., 1989); $u_{\theta RSS}$= $0.01U_m$, u_{rRSS}= $0.01U_m$, and u_{zRSS}= $0.04U_m$ in the θ, r, and z directions, respectively.

5. Reevaluation of turbulence statistics in square duct by Sata et al. (1994)

Sata et al. (1994) compared their 3-D PTV results in a straight square duct with their own HWA data, and confirm the reliability of their measurement technique. In this section, their measurement results with 3-D PTV are repeated and compared with the previous data. In their experiment, the hydraulic diameter H was 71 mm, and a test section was located $71H$ downstream from the inlet, where the flow was fully developed. The data set measured with bubbles is used for the present comparison. The centerline velocity was set to be U_0=5.0 m/s, which corresponds to Re_m=18900. The time interval between the strobo flashes was chosen as $\Delta t_1 = 960\mu s$ (see Fig. 2) , while the third flash in the latter image field was omitted. On average, 9 vectors were measured per frame, and 4x10^5 vectors in total were obtained. The number of velocity vectors in each data cell was 1000–1500.

Figure 10 shows contours of the streamwise mean velocity U nondimensionalized by U_m. The 3-D PTV data by Sata et al. (1994) are in good agreement with the LDA data of Brundrett and Baines (1964), although their Reynolds number (Re_m =83000) is much larger than that of Sata et al. (1994). Demuren and Rodi (1984) claimed that bulging of the velocity contours towards corner, which is caused by the secondary flow, becomes less evident, if the developing region is not long enough. The measurement result indicates that flow reaches a fully-developed state in the test section at $X/H = 71$.

Figure 11(a) shows the magnitude of the secondary flow along the corner bisector. The magnitude obtained by Sata et al. (1994) is about 1–1.5 % of U_m and in accordance with the LDA data of Brundrett and Baines (1964). The DNS data of Huser and Biringen (1993) at Re_m=10320 rapidly decrease near the center of the duct. Streamwise counter rotating vortices characterizing the flow are well captured as shown in Fig. 11(b). The center of the vortical motion is located at around $(y/(H/2), z/(H/2)) = (-0.75, -0.3)$. On the other hand, the DNS data of Huser and Biringen (1993) and Gavrilakis (1992) at lower Reynolds numbers give vortices located closer to the corner, i.e., at around $(y/(H/2), z/(H/2)) = (-0.5, -0.2)$, which is consistent with the smaller secondary flow near the center of the duct.

The rms velocity fluctuations along the wall bisectors are shown in Fig. 12. The data of Sata et al. (1994) are generally in good accordance with the HWA data of Fujita et al. (1989) at Re_m=65000 and the LDA data of Brundrett and Baines (1964).

Figure 13 shows contours of u_{rms}/U_m. As reported previously by several investigators, isolines of u_{rms} are distorted toward the corner

due to the secondary flow along the corner bisector. Again, the data of Sata et al. (1994) are in reasonable agreement with the data of Brundrett and Baines (1964), although contours of the former results are somewhat less distorted.

As a whole, the measurement data of Sata et al. (1994) in a straight air duct are in good accordance with the previous results, although the tracer particle employed does not have sufficient traceability to the turbulence micro scales, but to the energy containing turbulent scales. This fact encourages us to apply the 3-D PTV system to a turbulent air flow in a curved duct as shown in the following section.

6. Turbulence statistics in square cross-sectioned curved duct

In the present measurement, the bulk mean velocity U_m is 3.65 m/s, which corresponds to Re_m= 17400 and the Dean number defined by

$$De = \sqrt{H/(2R_c)} \tag{6}$$

is 6720. The time intervals between the strobo flashes are chosen as $\Delta t_1 = \Delta t_2 = 480\mu s$. Particle images are captured for about 24 minutes at each measurement volume. On average, 16 vectors per frame are measured, and 1.4x10^6 vectors in total were obtained. The sample size in each data cell is 200–800. Despite the relatively small sample size, the ensemble-averaged turbulence statistics reasonably converge as shown below, since the time period of the measurement is about 5 order of magnitudes larger than the largest time scale of the flow field.

Distributions of the mean tangential velocity U_θ at 90 degrees downstream of the bend inlet are shown in Fig. 14. A marked trough in U_θ is observed at a normal distance of about $0.3H$ from the inner wall as reported by Chang et al. (1983), although their Reynolds number is about 3 times larger than the present one. Note that the present data are larger in most part of the cross section than those of Chang et al. (1983). This discrepancy is partly due to some error in the bulk mean velocity they used, since they separately measured U_θ and U_m. On the other hand, U_m in the present study is determined by integrating U_θ over the bottom half of the cross-section; U_m thus obtained changes only by 0.1% at θ=89, 90, and 91 degrees.

Figures 15–17 show the distribution of the secondary flow in the cross-stream plane. A strong inward secondary flow as large as 0.1–$0.3U_m$ is found at $|z/(H/2)| > 0.8$, and it is compensated with the moderate outward flow of 0.05–$0.1U_m$ at $|z/(H/2)| < 0.6$. The vertical velocity U_z is negative at $r^* < 0.2$ and reaches its maximum value of

$0.2U_m$ near the inner wall. A large clockwise vortical structure can be seen in Fig. 15, while another small counter-clockwise vortex is also observed close to the centerline near the inner wall.

The divergence of the mean velocity vector D,

$$D = \frac{1}{r}\frac{\partial U_\theta}{\partial \theta} + \frac{U_r}{r} + \frac{\partial U_r}{\partial r} + \frac{\partial U_z}{\partial z}, \tag{7}$$

is calculated by using a 2nd-order central difference scheme on the present data cells, and nondimensionalized with the magnitude of the inflow rate per unit volume,

$$M = \{|U_\theta \Delta r \Delta z| + |U_r r \Delta\theta \Delta z| + |U_z r \Delta\theta \Delta r|\}/(r\Delta\theta\Delta r\Delta z). \tag{8}$$

Although it is not shown here, D/M is found to be less than 0.04 except in the vicinity of the inner and outer walls, where the accuracy of the velocity gradients is deteriorated. Therefore, the mean velocity field presently obtained satisfies the continuity equation reasonably well.

Huser et al. (1994) reported that the distributions of the Reynolds stress budget terms remain unchanged in the straight duct except near the corner. However, this is not the case for the curved duct due to the presence of the strong secondary flow; the turbulent fluctuations are significantly increased especially away from the duct wall. Figures 18–20 show the distribution of RMS velocity fluctuations. For an incompressible flow of constant physical properties, the production terms in the Reynolds normal stress transport equations in the cylindrical coordinates lead to

$$P_{\theta\theta} = -2\overline{u_\theta^2}\frac{1}{r}(\partial U_\theta/\partial\theta + U_r) - 2\overline{u_\theta u_r}(\partial U_\theta/\partial r) - 2\overline{u_\theta u_z}(\partial U_\theta/\partial z), \tag{9}$$

$$P_{rr} = -2\overline{u_\theta u_r}\frac{1}{r}(\partial U_r/\partial\theta - U_\theta) - 2\overline{u_r^2}(\partial U_r/\partial r) - 2\overline{u_r u_z}(\partial U_r/\partial z), \tag{10}$$

and

$$P_{zz} = -2\overline{u_\theta u_z}\frac{1}{r}(\partial U_z/\partial\theta) - 2\overline{u_r u_z}(\partial U_z/\partial r) - 2\overline{u_z^2}(\partial U_z/\partial z). \tag{11}$$

In the present study, each term in Eqs. (9)–(11) is evaluated and its contribution to the total production rate is examined. Note that the third order spline functions are employed to smooth irregular data points in the distributions of the turbulent statistics when the budget terms are calculated. Figure 21 shows contours of the production terms $P_{\theta\theta}$, P_{rr}, and P_{zz} nondimensionalized with (U_m^3/H).

Among the production terms in the θ direction, the shear production terms of $-2\overline{u_\theta u_r}(\partial U_\theta/\partial r)$ and $-2\overline{u_\theta u_z}(\partial U_\theta/\partial z)$ are dominant near the side and bottom walls, respectively and $u_{\theta,rms}$ becomes large near the

wall as shown in Fig. 18. The magnitude of $u_{\theta,rms}$ near the outer wall is larger than that near the inner wall, and this tendency is pronounced near the symmetry plane (z=0). On the other hand, due to the trough in U_θ, there exists regions of large $\partial U_\theta/\partial r$ or $\partial U_\theta/\partial z$ at $|z/(H/2)| < 0.5$ and $r^* < 0.5$, where $u_{\theta,rms}$ is increased. A peak in $u_{\theta,rms}$ at r^*=0.4–0.45 near the symmetry plane is also observed by Chang et al. (1983). In the radial direction, $-2\overline{u_r u_z}(\partial U_r/\partial z)$ is dominant near the bottom wall due to the strong inward secondary motion, while $-2\overline{u_r^2}(\partial U_r/\partial r)$ becomes large near the outer wall. As a result, $u_{r,rms}$ is as large as $0.1U_m$ in these regions, but it is decreased near the inner wall due to the negative production $-2\overline{u_r^2}(\partial U_r/\partial r)$ there. The present data near the symmetry plane are much larger than those of Chang et al. (1983). It is also noted that the local minimum of their data in $u_{r,rms}$ is not reproduced in the present experiment. Since $-2\overline{u_z^2}(\partial U_z/\partial z)$ becomes large near the inner wall, $u_{z,rms}$ is markedly increased at $r^* < 0.3$. This is the opposite trend to the other two components. On the other hand, $-2\overline{u_z^2}(\partial U_z/\partial z)$ is negative near the outer wall, where large magnitude of $u_{z,rms}$ might be maintained though the convection and/or pressure-strain correlation terms.

Figure 22 shows the distributions of the Reynolds shear stress. In the straight duct (Sata et al., 1994), $\overline{u_x u_z}$ is positive at $r^* > 0.5$ and negative at $r^* < 0.5$ as in the fully-developed turbulent channel flow. In the curved duct, however, $\overline{u_\theta u_r}$ exhibits a different trend; $\overline{u_\theta u_r}$ is positive in the most part of the duct and becomes markedly large near the outer wall. On the other hand, the other components $\overline{u_\theta u_z}$ and $\overline{u_r u_z}$ are positive near the outer and bottom walls and negative near the inner wall, respectively. The region of large negative $\overline{u_\theta u_z}$ at around $(r^*, z/(H/2)) = (0.4, 0.3)$ leads to the substantial production in the tangential direction as shown in Fig. 21(a).

Figure 23 shows the profiles of the second and third invariants of the anisotropy tensor (Lumley, 1978), which are defined as:

$$II = -b_{ij}b_{ji}/2, \tag{12}$$

and

$$III = b_{ij}b_{jk}b_{ki}/3, \tag{13}$$

where,

$$b_{ij} = \overline{u_i u_j}/\overline{u_k u_k} - \delta_{ij}/3 \tag{14}$$

The third invariant is positive in most of the flow domain, which corresponds to the nozzle-type flow (Lumley, 1978). In the straight duct (Sata et al., 1994), II and III respectively become large negative and positive values near the wall, so that the flow field approaches to one-component turbulence toward the wall. The flow field becomes almost

isotropic in the center of the duct, where the absolute values of II and III are small. In the curved duct, the behavior of II and III near the inner and bottom wall is similar with that in the straight duct, while their magnitude is somewhat decreased near the outer wall. On the other hand, the flow field near the symmetry plane around r^*=0.4–0.45 becomes more anisotropic due to the large production of $u_{\theta,rms}$ in this region.

Figure 24 shows contours of the flatness parameter A (Lumley, 1978),

$$A = 1 + 9II + 27III. \tag{15}$$

In the straight duct (Sata et al., 1994), A becomes somewhat large along the corner bisectors, while the contours near the wall are almost parallel to the wall. On the other hand, the distribution of A in the curved duct exhibits a different trend; there exists a local minimum in A near the center of the duct. At r^*=0.1–0.2 and $|z/(H/2)|$=0.6–0.8, A becomes as large as 0.9, the flow field near the corner of the inner-wall side is close to isotropic.

7. Conclusion

A three-dimensional particle tracking velocimeter was applied to the turbulent air fow measurement in a strongly curved U-bend. He-filled soap bubbles were employed as a flow tracer in order to reduce the unwanted effect of the centrifugal force on particle trajectory. Turbulent statistics measured are generally in good accordance with the LDA data of Chang et al. (1983) at higher bulk-mean Reynolds number. Each production term in the Reynolds normal stress transport equations were evaluated, and the production mechanism of the turbulence kinetic energy was examined. In the tangential direction, substantial production exists near the symmetry plane as well as near the wall. The horizontal and vertical components also have large production induced by the strong secondary flow near the bottom and inner walls, respectively. Therefore, the distributions of invariants of the stress anisotropy tensor are markedly modified in the curved duct, i.e., the region near the symmetry plane becomes more anisotropic, while the region near the inner corner is close to an isotropic state.

Acknowledgements

The authors are greteful to Dr. Yutaka Sata at Toshiba Co., Ltd., and Dr. Kazuho Sato at Calsonic Corp. for their valuable discussion and coorporation during the course of this work.

References

R. J. Adrian. Particle-imaging techniques for experimental fluid mechanics. *Annu. Rev. Fluid Mech.*, 23:261–304, 1991.

T. Adachi, K. Nishino and K. Torii. Digital PTV measurements of a separated air flow behind a backward-facing step. *J. Flow Vis. Image Proc.*, 1:317–335, 1993.

J. Azzola, J. A. C. Humphrey, H. Iacovides and B. E. Launder. Developing turbulent flow in a U-bend of circular cross-section: measurement and computation. *ASME J. Fluid Eng.*, 108:214–221, 1986.

ANSI/ASME PTC 19.1-1985. *Measurement uncertainty, supplement on instruments and apparatus, part 1.* 1987.

E. Brundrett and W. D. Baines The production and diffusion of vorticity in a square duct. *J. Fluid Mech.*, 19:375–394, 1964.

S. M. Chang, J. A. Humphrey and A. Modavi. Turbulent flow in a strongly curved U-bend and downstream tangent of square cross-sections. *Physico Hydrodyn.*, 4:243–269, 1983.

Y. D. Choi, C. Moon and S. H. Yang. Measurement of turbulent flow characteristics of square duct with a 180 bend by hot-wire anemometers. *Proc. Int Symp. Eng. Turbulence Modelling and Meas.*, 429–439, Dubrovnik, Yugoslavia, 1990.

R. Clift, J. R. Grace and M. E. Weber. *Bubbles, drops and particles.* Academic Press, New York, 1978.

A. O. Demuren and W. Rodi. Calculation of turbulence-driven secondary motion in non-circular ducts. *J. Fluid Mech.*, 140:189–222, 1984.

H. Fujita, M. Hirota, H. Yokosawa and S. Iwata. Measurement of turbulent flow in a square duct with roughenedwalls on two opposite sides. *Int. J. Heat & Fluid Flow*, 10:125–130, 1989.

S. Gavrilakis. Numerical simulation of low-Reynolds-number turbulent flow through a straight square duct. *J. Fluid Mech.*, 244:101–129, 1992.

Y. G. Guezennec, R. S. Brodkey, N. Trigui and J. C. Kent. Algorithms for fully automated three-dimensional particle tracking velocimetry. *Exp. Fluids*, 17:209–219, 1994.

J. A. C. Humphrey, J. H. Whitelaw and G. Yee. Turbulent flow in a square duct with strong curvature. *J. Fluid Mech.*, 103:443–463, 1981.

A. Huser and S. Biringen. Direct numerical simulation of turbulent flow in a square duct. *J. Fluid Mech.*, 257:65–95, 1993.

A. Huser, S. Biringen and F. F. Hatay. Direct simulation of turbulent flow in a square duct: Reynolds-stress budgets. *Phys. Fluids*, 6:3144–3152, 1994.

H. Iacovides, B. E. Launder, P. A. Loizou and H. H. Zhao. Turbulent boundary-layer development around a square-sectioned U-bend: Measurements and Computation. *ASME J Fluid Eng.*, 112:409–415, 1990.

H. Ito. Friction factors for turbulent flow in curved pipes. *ASME J Basic Eng.*, 81:123–134, 1959.

N. Kasagi and K. Nishino. Probing turbulence with three-dimensional particle-tracking velocimetry. *Exp. Thermal Fluid Sci.*, 4:601–610, 1992.

N. Kasagi and Y. Sata. Recent developments in three-dimensional particle tracking velocimetry. *Proc. 6th Int. Symp. Flow Vis.*, 832–837, Yokohama, 1992.

N. Kasagi and A. Matsunaga. Three-dimensional particle-tracking velocimetry measurement of turbulence statistics and energy budget in a backward-facing step flow. *Int. J. Heat and Fluid Flow*, 16:477–485, 1995.

H. Kato, K. Ninisho and K. Torii. 3-D PTV measurement of an air turbulent flow. *J. Vis. Soc. Jpn.*, 12 Suppl.:111–114, in Japanese, 1992.

J. C. Kent and A. R. Eaton. Stereo photography of neutral density He-filled bubbles for 3-D fluid motion studies in an engine cylinder. *Applied Optics*, 21:904–912, 1982.

J. L. Lumely. Computational modeling of turbulent flows. *Adv. Appl. Mech.*, 18:123–176, 1978.

H. G. Maas, A. Gruen and D. A. Papantoniou. Particle tracking velocimetry in three-dimensional flows: Part I. Photogrammetric determination of particle coordinates. *Exp. Fluids*, 15:133–146, 1993.

N. A. Malik, Th. Dracos and D. A. Papantoniou. Particle tracking velocimetry in three-dimensional flows: Part II. Particle Tracking. *Exp. Fluids*, 15:279–294, 1993.

R. Mei. Velocity fidelity of flow tracer particles. *Exp. Fluids*, 22:1–13, 1996.

A. Melling and J. H. Whitelaw. Turbulent flow in a rectangular duct. *J. Fluid Mech.*, 78:289–315, 1976.

A. Melling. Tracer particles and seeding for particle image velocimetry. *Meas. Sci. and Tech.*, 8:1406–1416, 1997.

N. Ninomiya and N. Kasagi. Measurement of the Reynolds stress budgets in an axisymmetric free jet with the aid of three-dimensional particle tracking velocimetry. *Proc. 9th Symp. Turbulence Shear Flows*, Kyoto, 6.1.1–6.1.6, 1993.

K. Nishino, N. Kasagi and M. Hirata. Three-dimensional particle tracking velocimety based on automated digital image processing. *ASME J. Fluid Eng.*, 111:384–391, 1989.

K. Nishino and N. Kasagi. Turbulence statistics measurement in a two-dimensional channel flow using a three-dimensional particle tracking velocimetry. *Proc. 7th Symp. Turbulence Shear Flows*, Stanford, 22.1.1–22.1.6, 1989.

T. R. Oakley, E. Loth and R. J. Adrian. Two-phase cinematic PIV method for bubbly flows. *ASME J. Fluid Eng.*, 119:707-712, 1997.

H. J. Perkins. The formation of streamwise vorticity in turbulent flows. *J. Fluid Mech.*, 44:721–740, 1970.

Y. Sata and N. Kasagi. Improvement toward high measurement resolution in three-dimensional particle tracking velocimetry. *Flow Visualization VI*, Y. Tanida et al., eds., Springer-Verlag, 792–796, 1992.

Y. Sata, K. Sato, N. Kasagi and N. Takamura. Application of the three-dimensional particle tracking velocimeter to a turbulent air flow. *Proc. 3rd Asian Symp. on Visualization*, Y. Nakayama et al., eds., Springer-Verlag, 705–709, 1994; also *Trans JSME, Ser. B.*, 60-571, 865–871, 1994, (in Japanese).

Y. Sata and N. Kasagi. Simultaneous measurement of three-dimensional object motion/deformation and circumambient fluid flow. *Flow Visualization VII*, J. Crowder et al., eds, Springer-Verlag, 721–726, 1995.

K. Sudo, M. Sumida and H. Hibara. Experimental investigation on turbulent flow in a circular-sectioned 90-degree bend. *Exp. in Fluids*, 25:42–49, 1998.

Y. Suzuki and N. Kasagi. On the turbulent drag reduction mechanism above a rblet surface. *AIAA J.*, 32: 1781–1790, 1994.

Y. Suzuki, M. Ikenoya and N. Kasagi. Three-dimensional PTV Measurement of the Phase Relationship Between Coherent Structures and Dispersed Particles in a Turbulent Channel Flow. *3rd Int. Workshop on Particle Image Velocimetry*, 107–112, 1999.

A. M. K. P. Taylor, J. H. Whitelaw, and M. Yianneskis. Curved ducts with strong secondary motion: velocity measurements of developing laminar and turbulent flow. *ASME J. Fluid Eng.*, 104:350–359, 1982.

	Plastic Capsule	Bubble
Density Ratio to Air	~30	~1
Diameter	< 100μm	0.5~1mm
Tracer Image	Clear	Two Peaks in brightness
Drawback	Adhesion to wall	Limitation in number density

Table 1 Characteristics of tracer particles

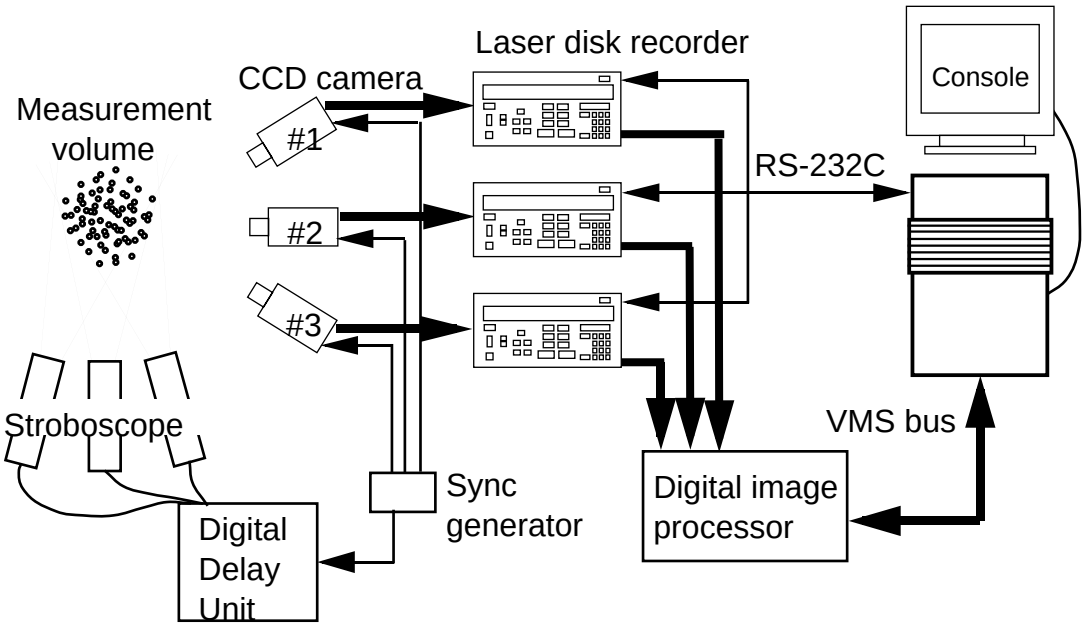

Fig. 1 3-D PTV system

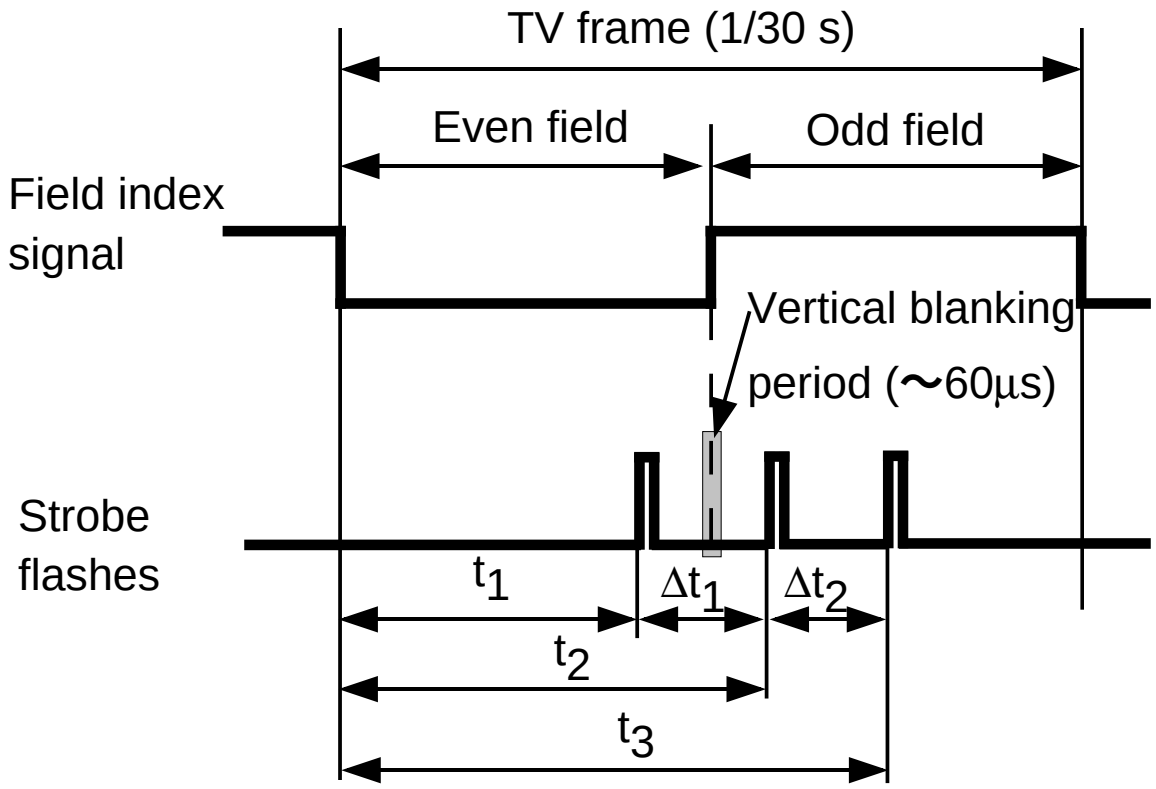

Fig. 2 Time sequence of the image acquisition

(a)

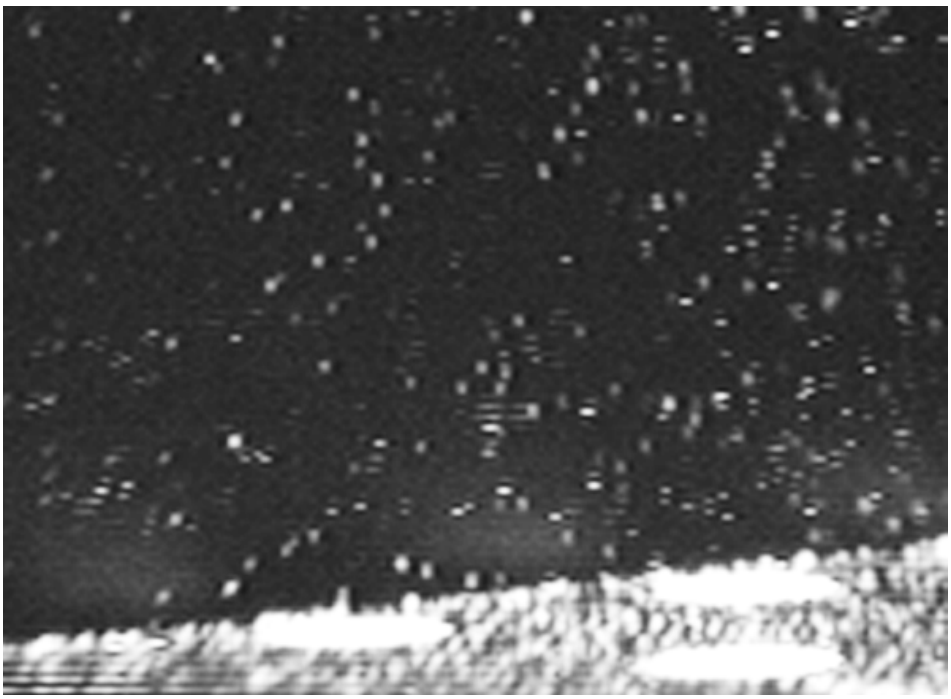

(b)

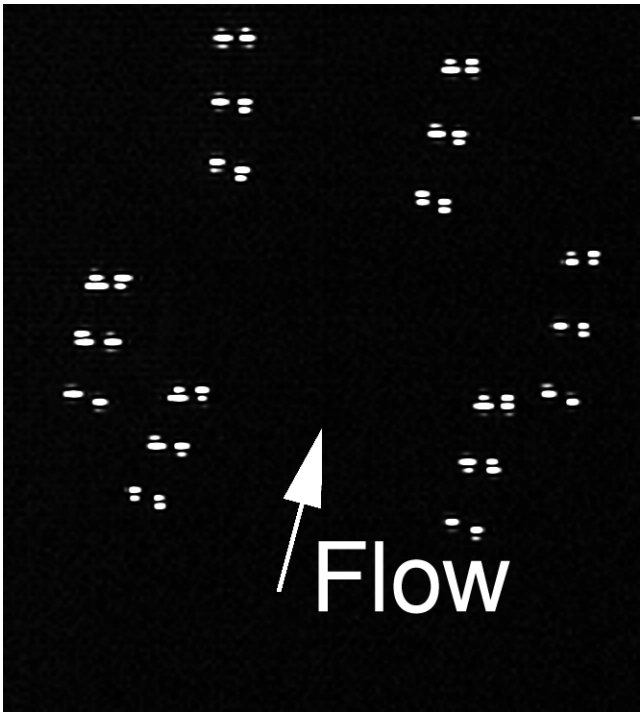

Fig. 3 Typical raw image of particles. (a) Plastic capsules (Sata et al., 1994), (b)Bubble particles.

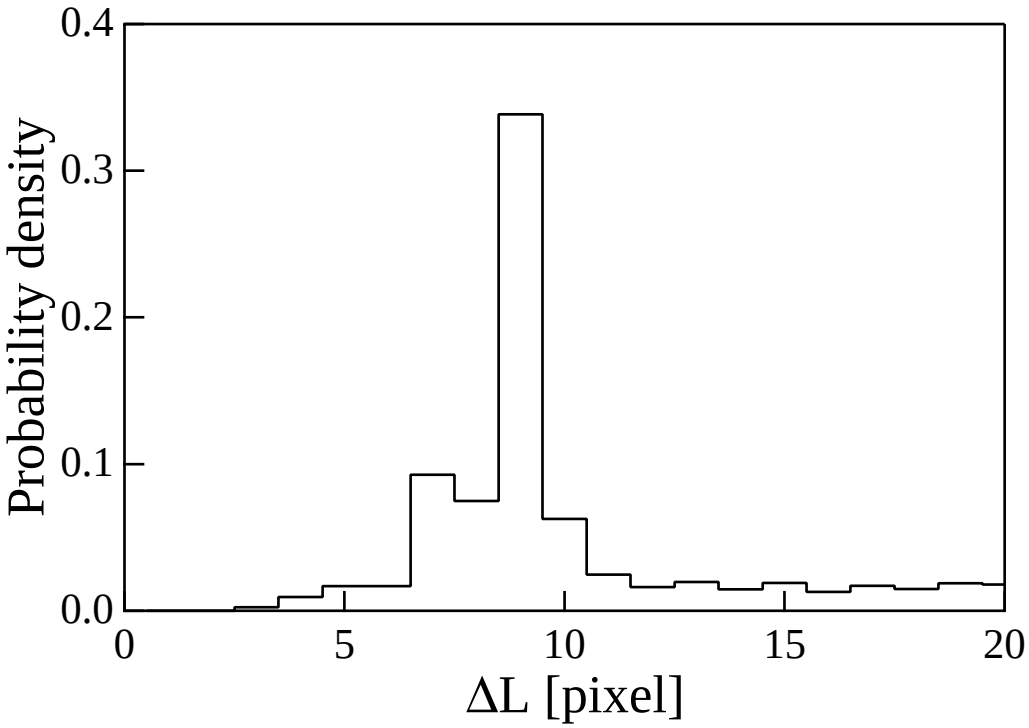

Fig. 4 Probability density of distance between a pair of brightness peaks.

(a)

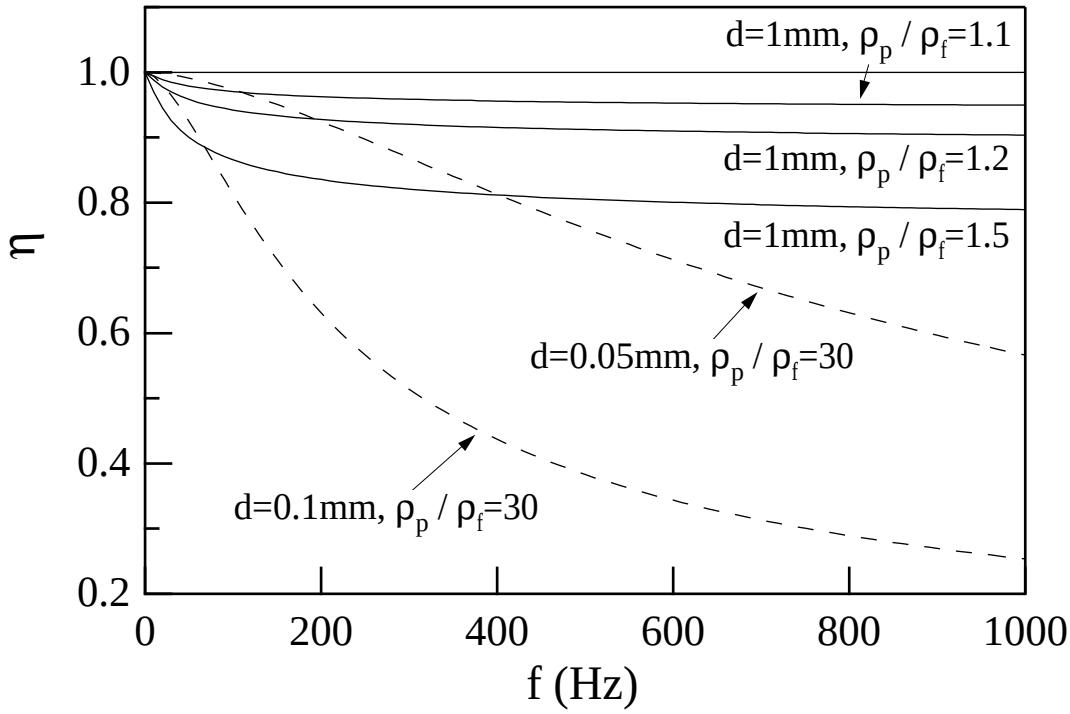

(b)

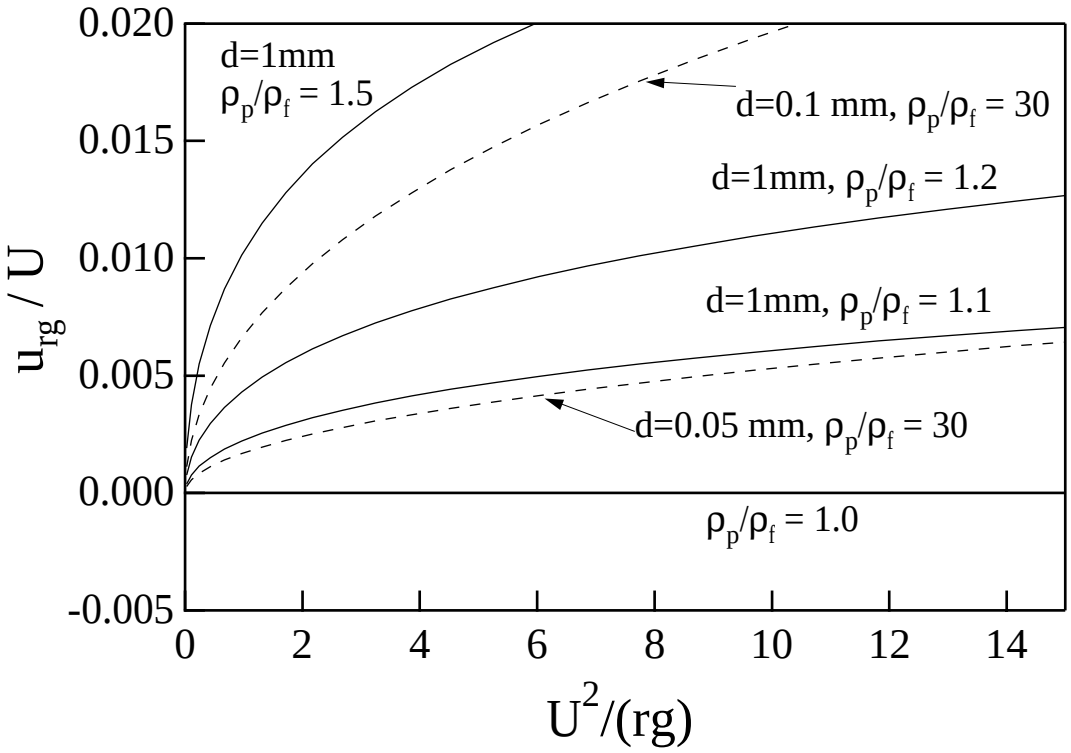

Fig. 5 Particle traceability. (a)Particle response in one-dimensional oscillating flow, (b)Radial velocity of tracers in curved flow.

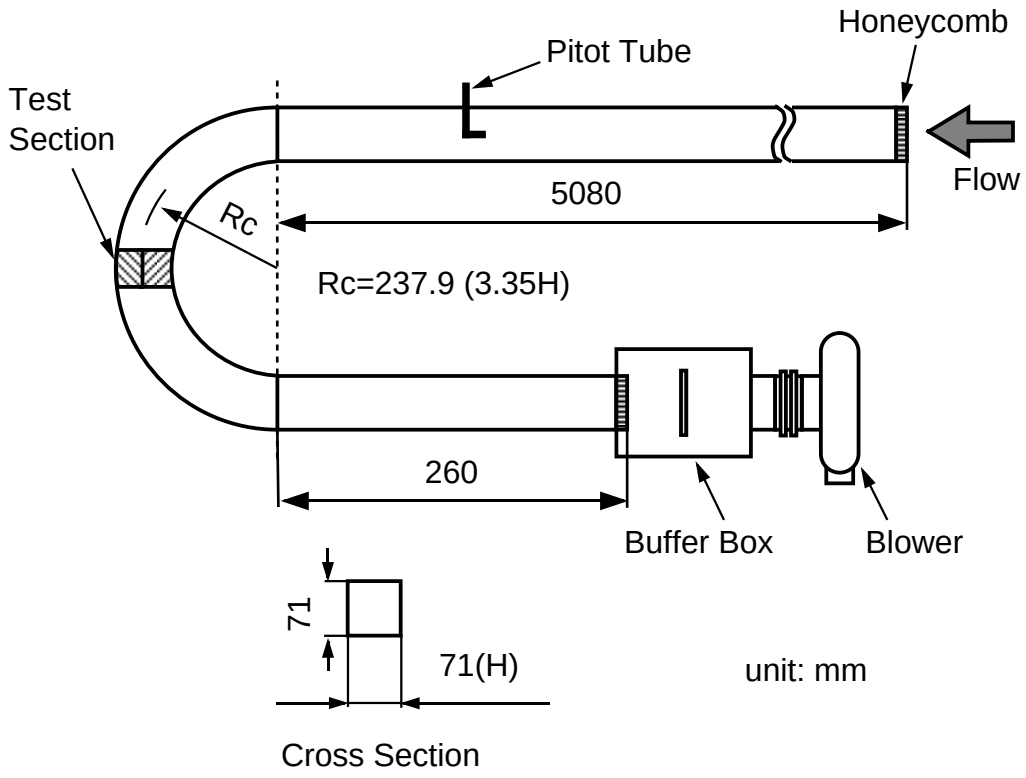

Fig. 6 Experimental setup.

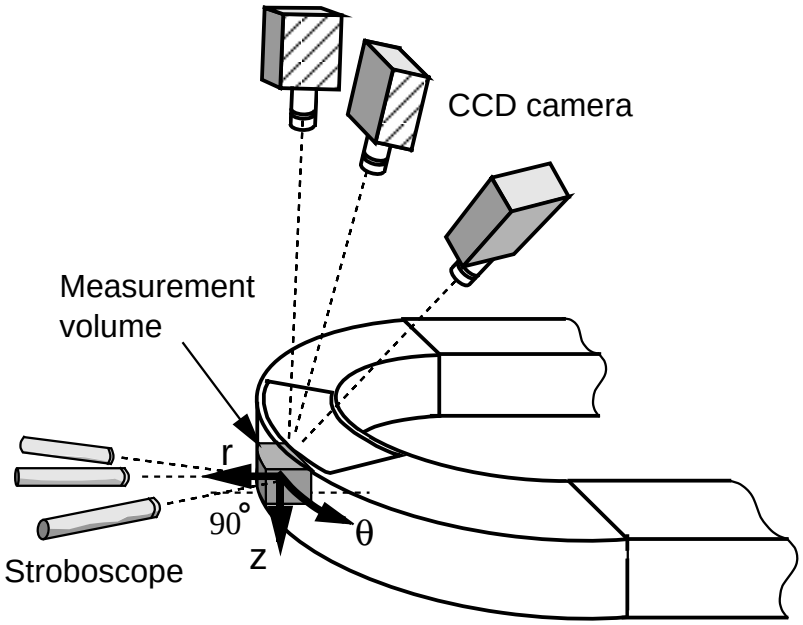

Fig. 7 Test section and camera setup for the curved duct.

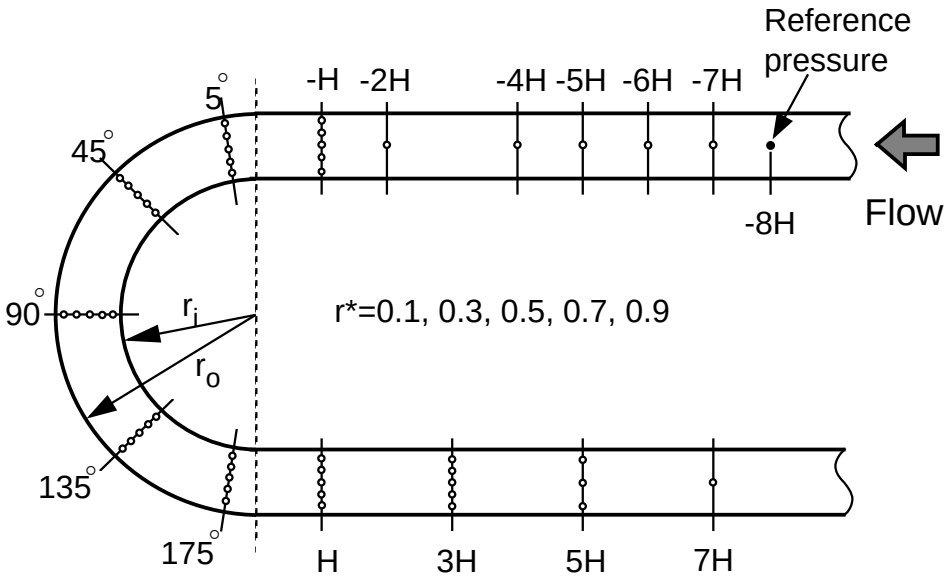

Fig. 8 Pressure tap locations in the curved duct.

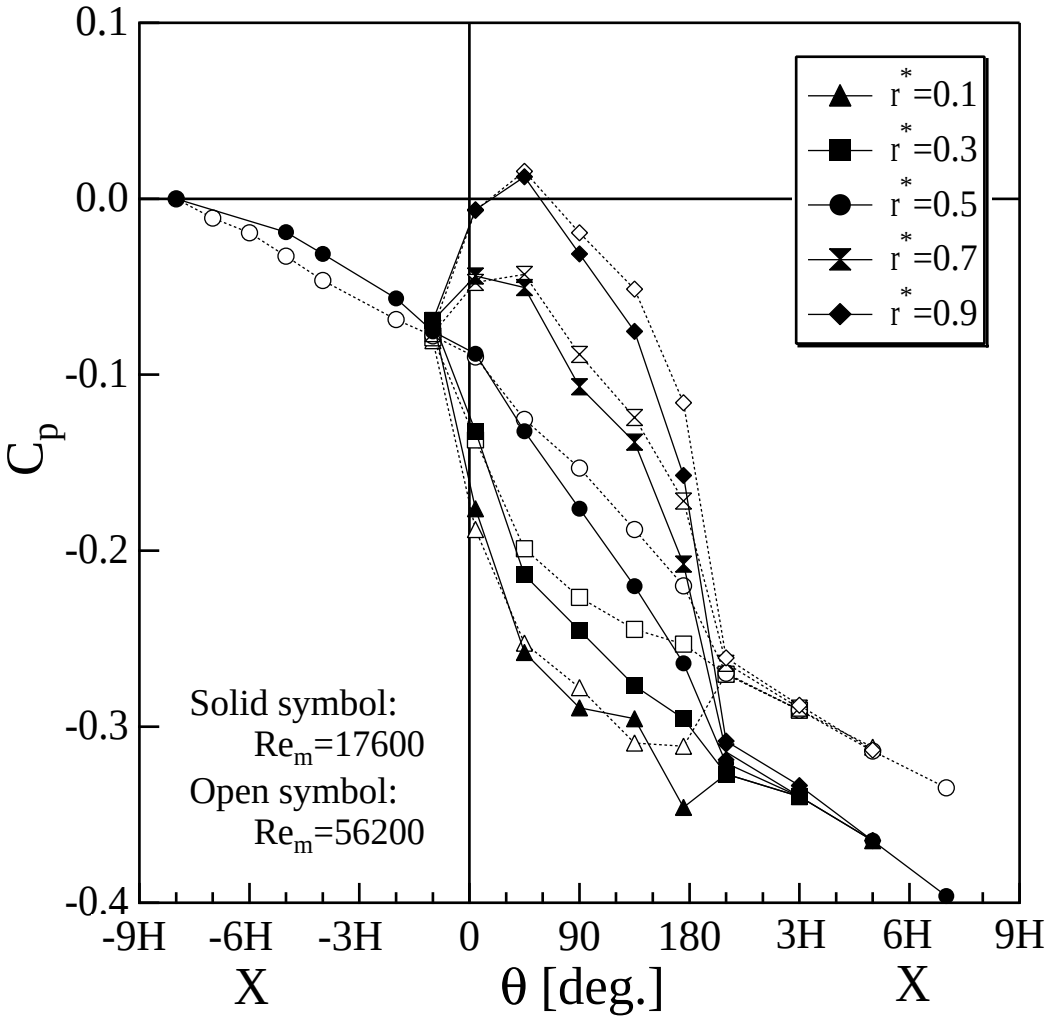

Fig. 9 Streamwise distribution of pressure coefficient in the curved duct.

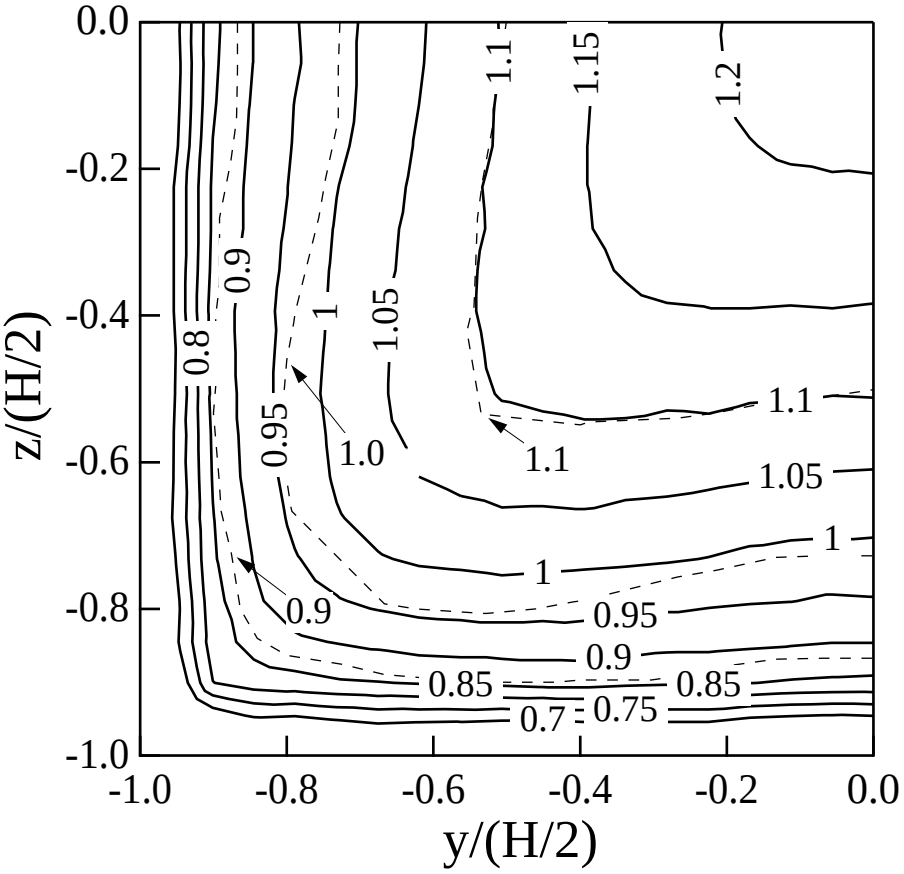

Fig. 10 Contours of mean streamwise velocity *U* (Sata et al., 1994).. Broken contours denote data by Brundrett & Baines (1964).

(a)

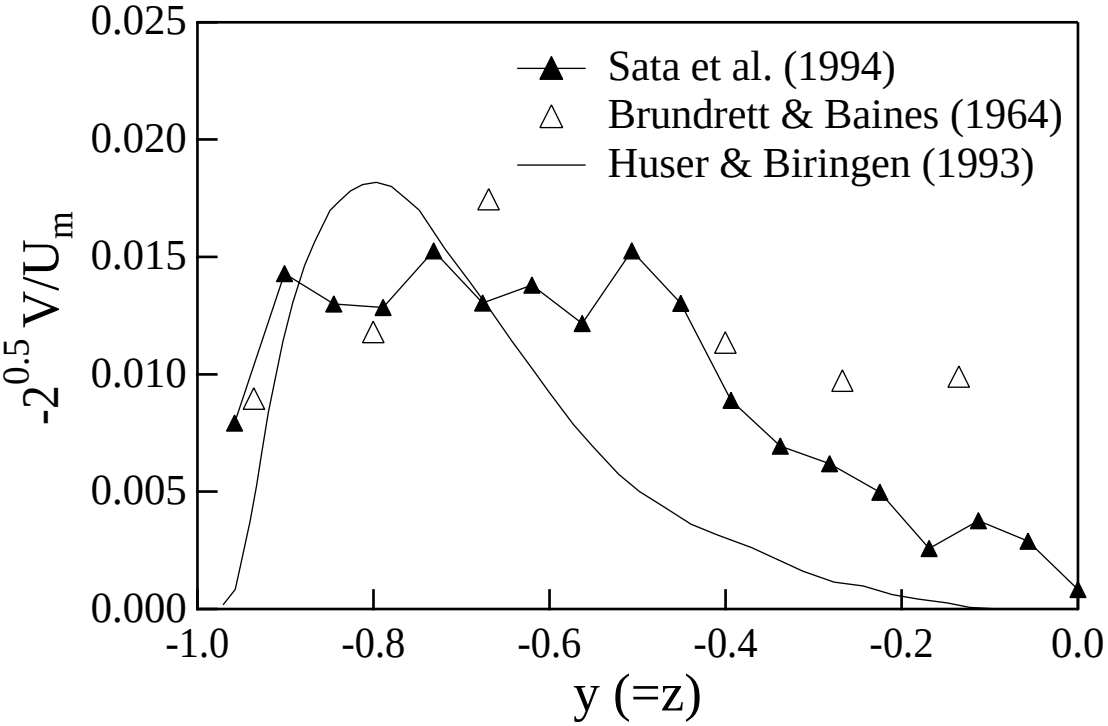

(b)

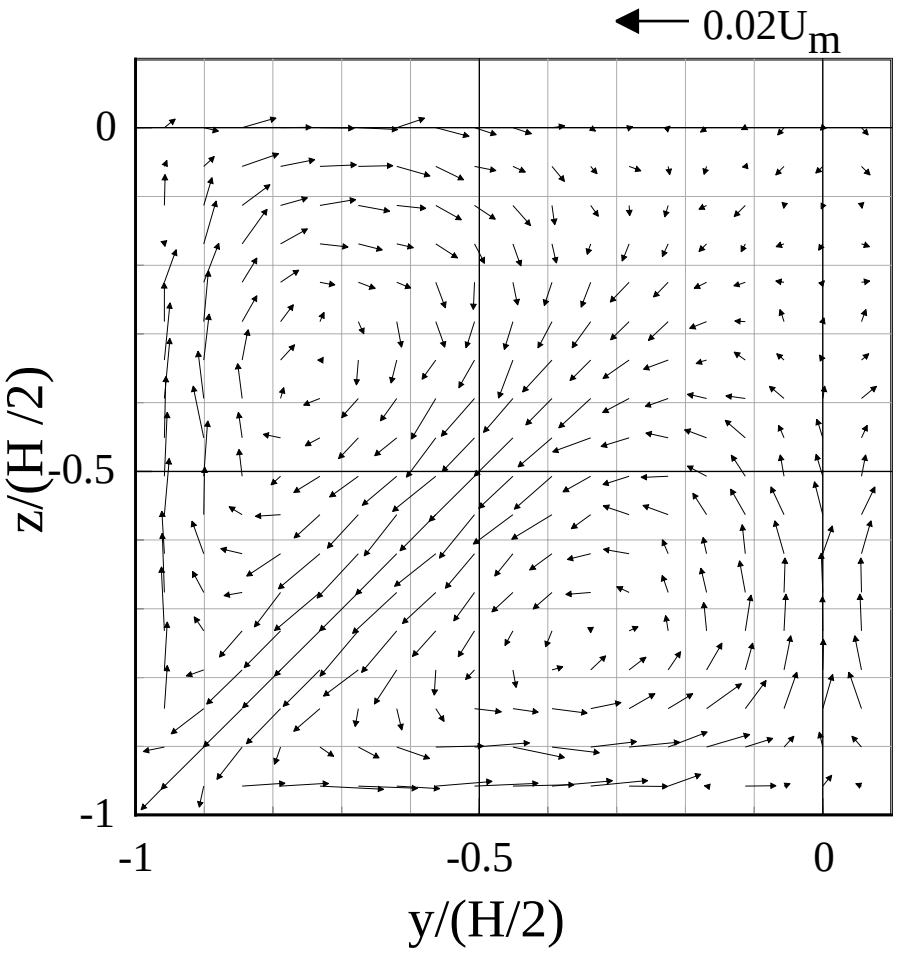

Fig. 11 Mean velocity in the cross stream plane (Sata et al., 1994). (a)Magnitude of the secondary flow along the corner bisector, (b)Secondary velocity vectors.

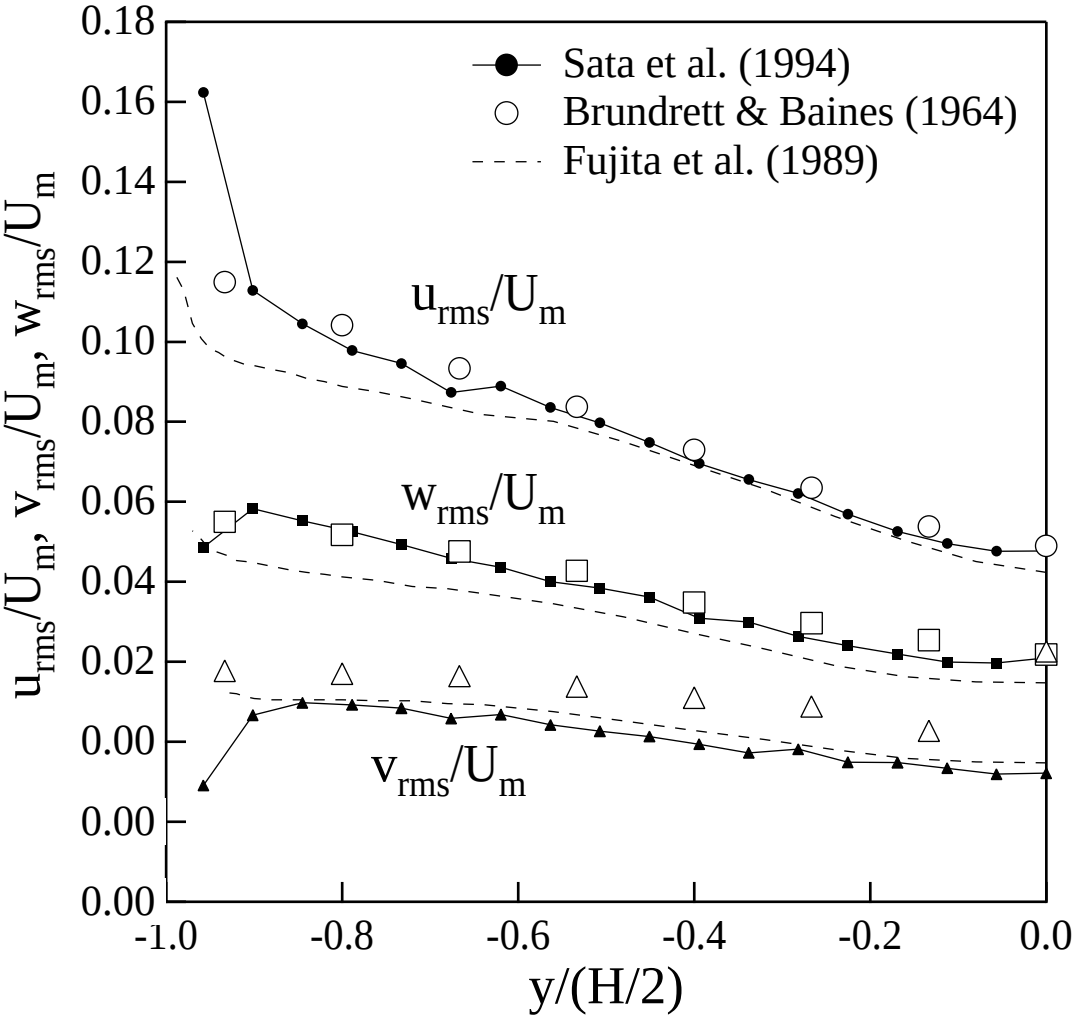

Fig.12 Distributions of velocity fluctuations along the wall bisector.

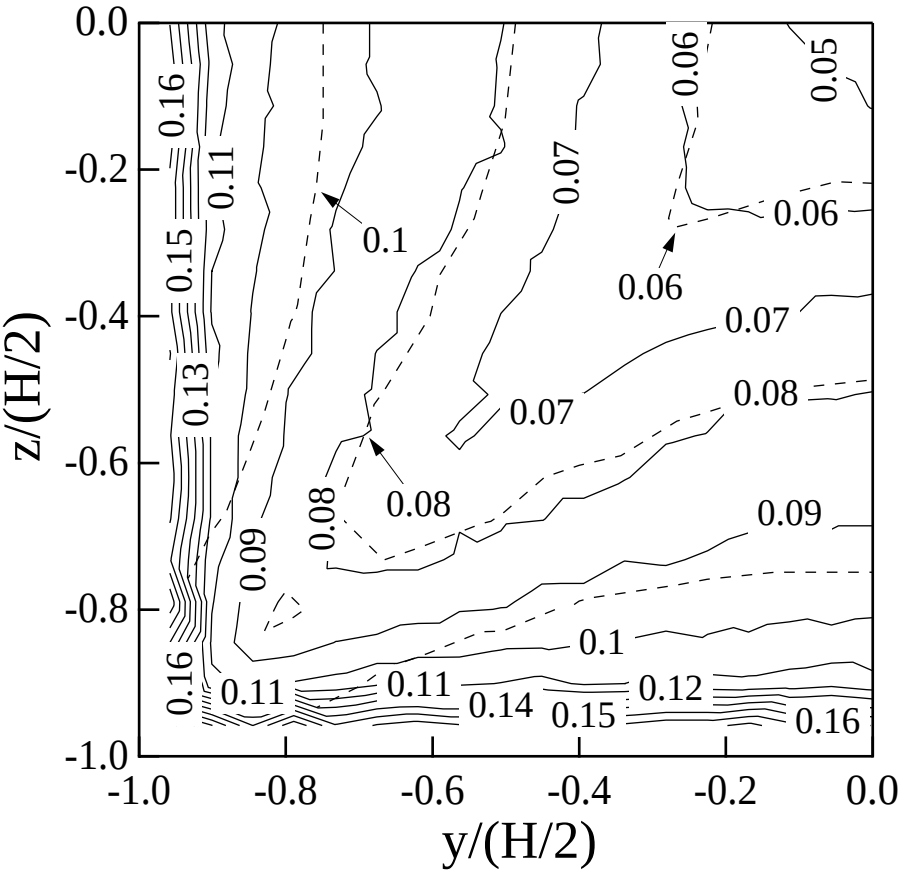

Fig. 13 Contours of streamwise RMS velocity fluctuation u_{rms}/U_m (Sata et al., 1994). Broken contours denote data by Brundrett & Baines (1964).

(a)

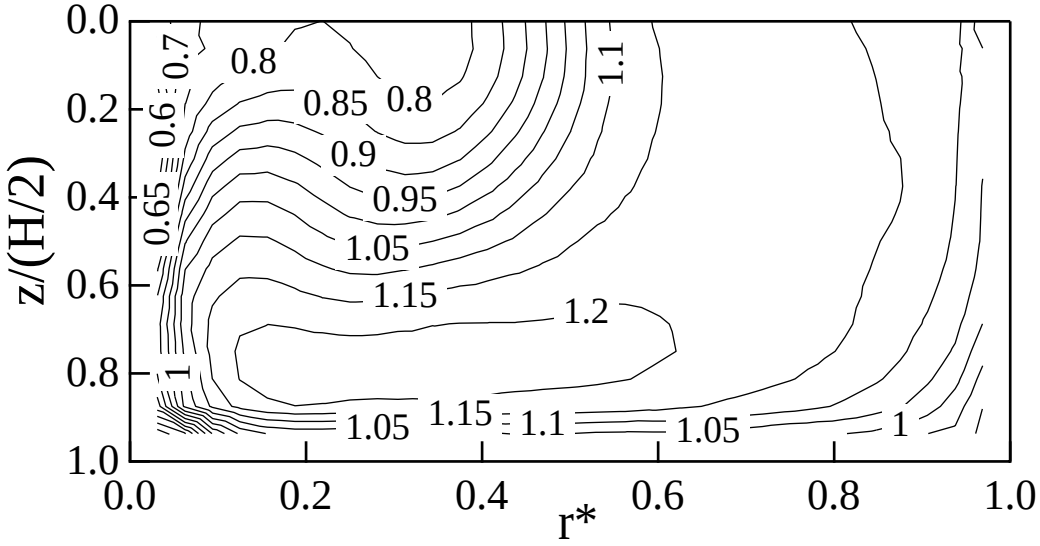

(b)

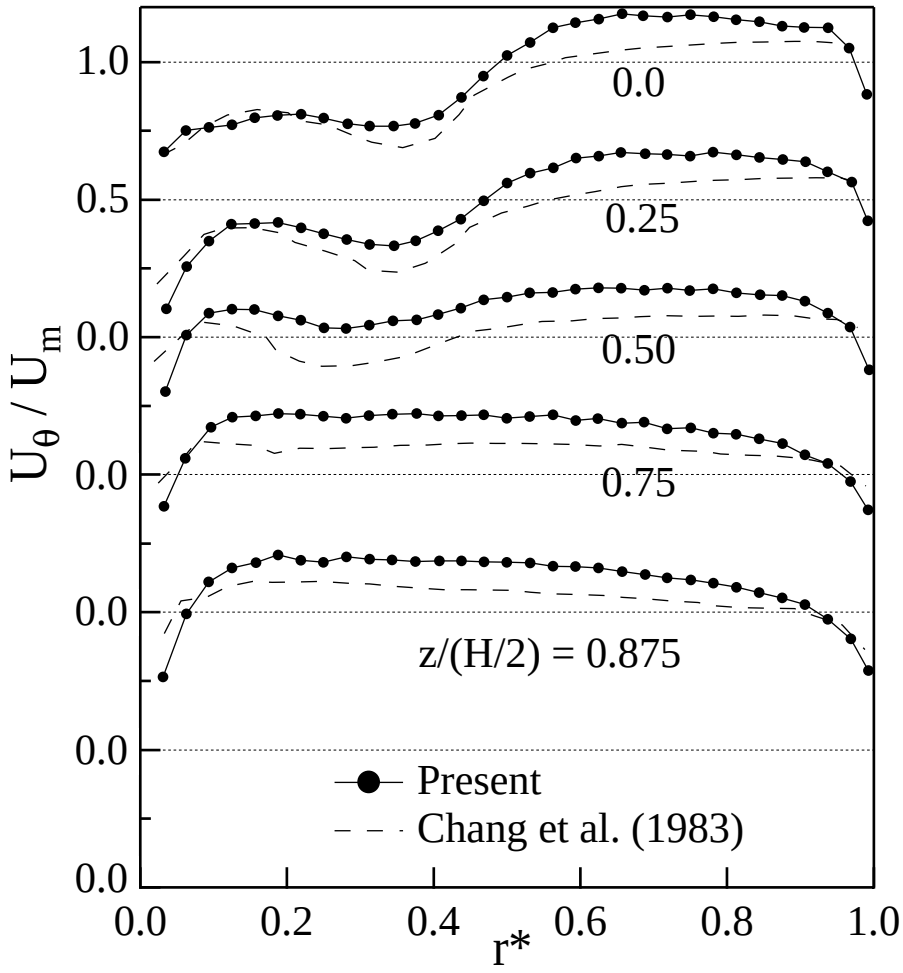

Fig. 14 Mean tangential velocity. (a)Contours, (b)Velocity profiles at five elevations from the bottom wall.

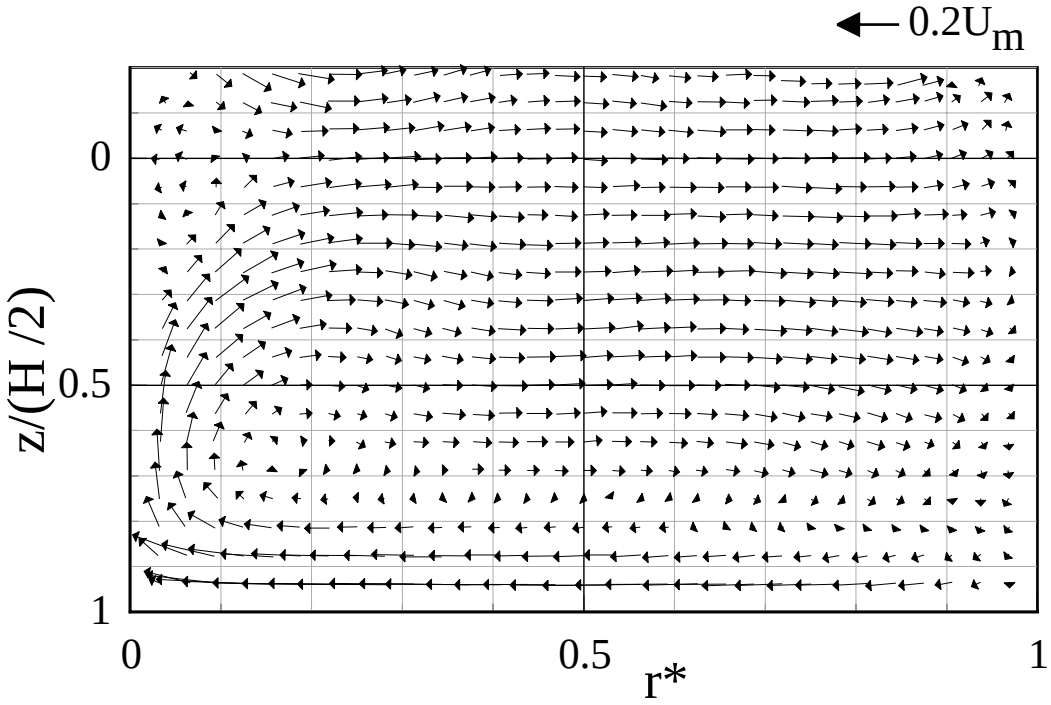

Fig. 15 Mean velocity vectors in the cross-stream plane.

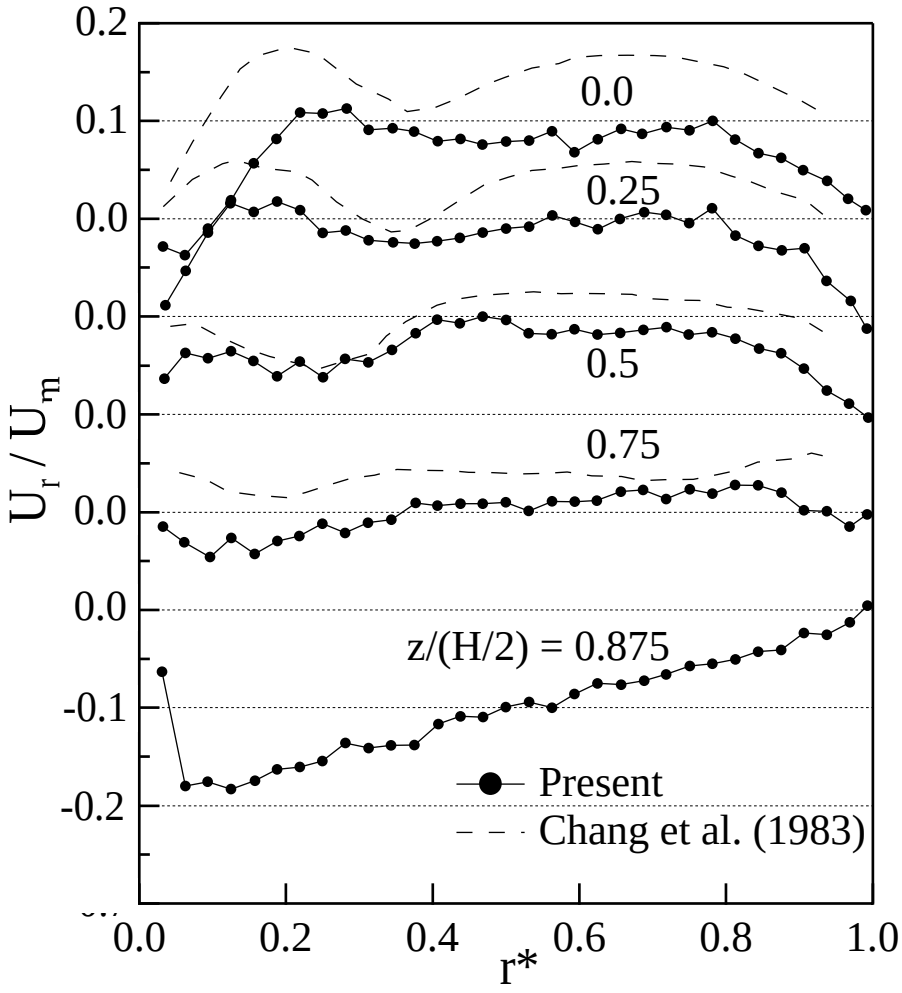

Fig. 16 Mean radial velocity profiles at five elevations from the bottom wall.

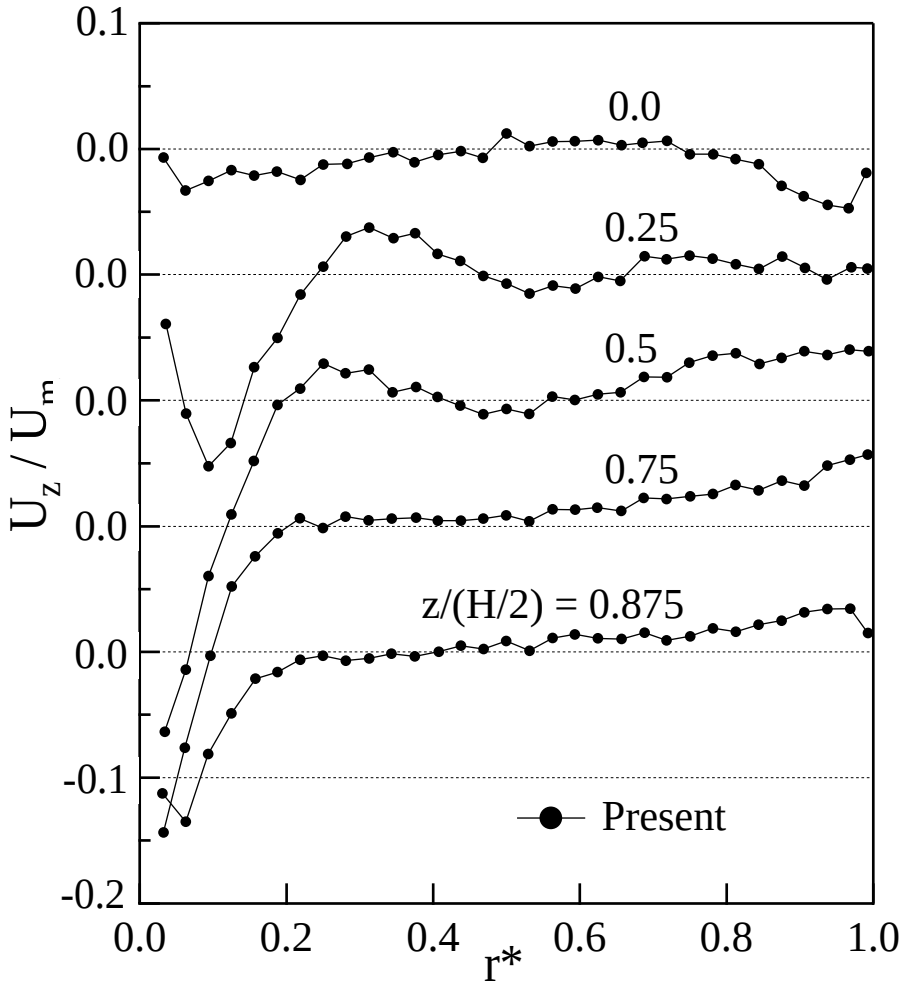

Fig. 17 Mean vertical velocity profiles at five elevations from the bottom wall.

(a)

(b)

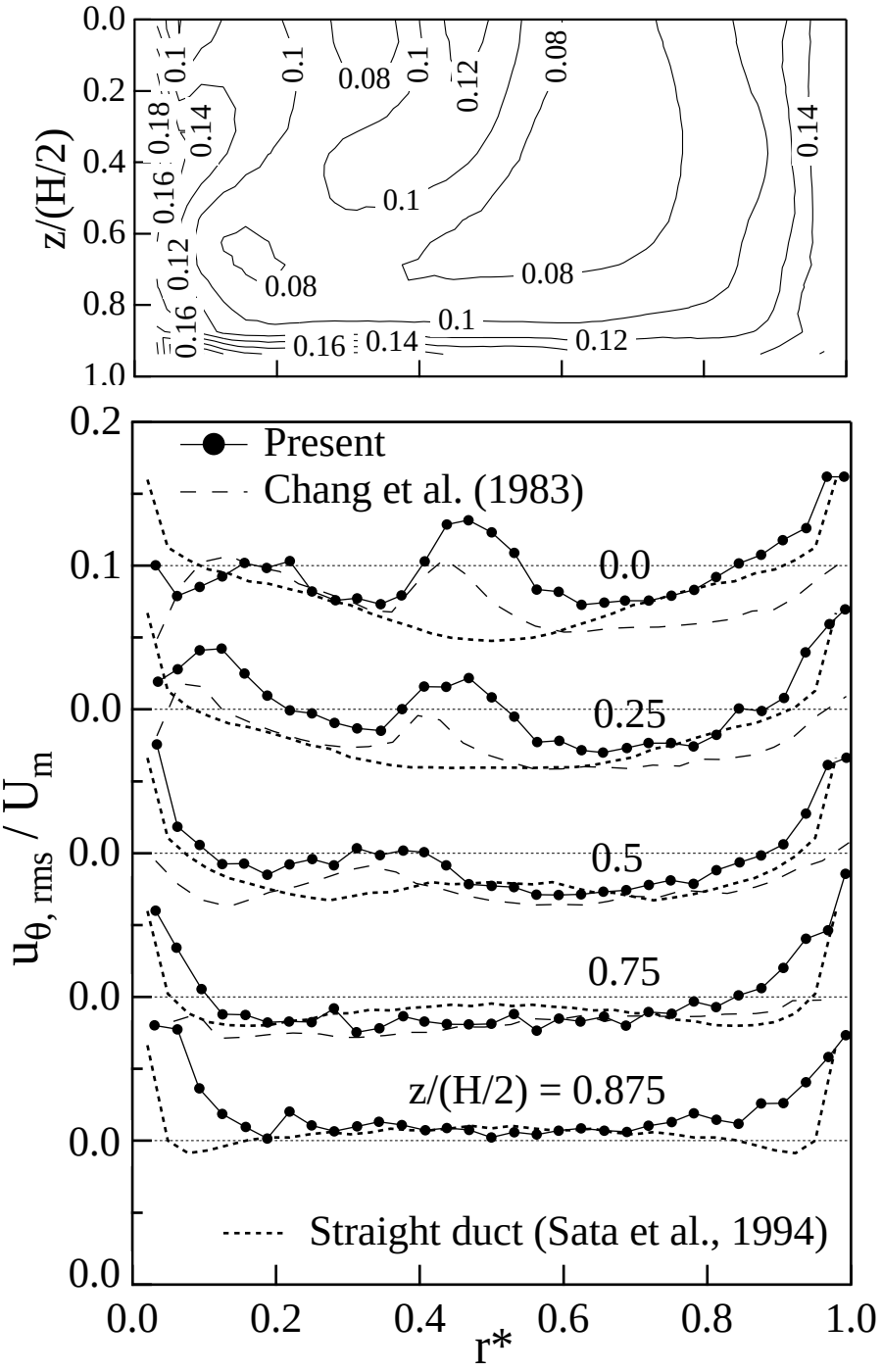

Fig. 18 Distributions of tangential RMS velocity fluctuations. (a)Contours, (b)Profiles at five elevations from the bottom wall.

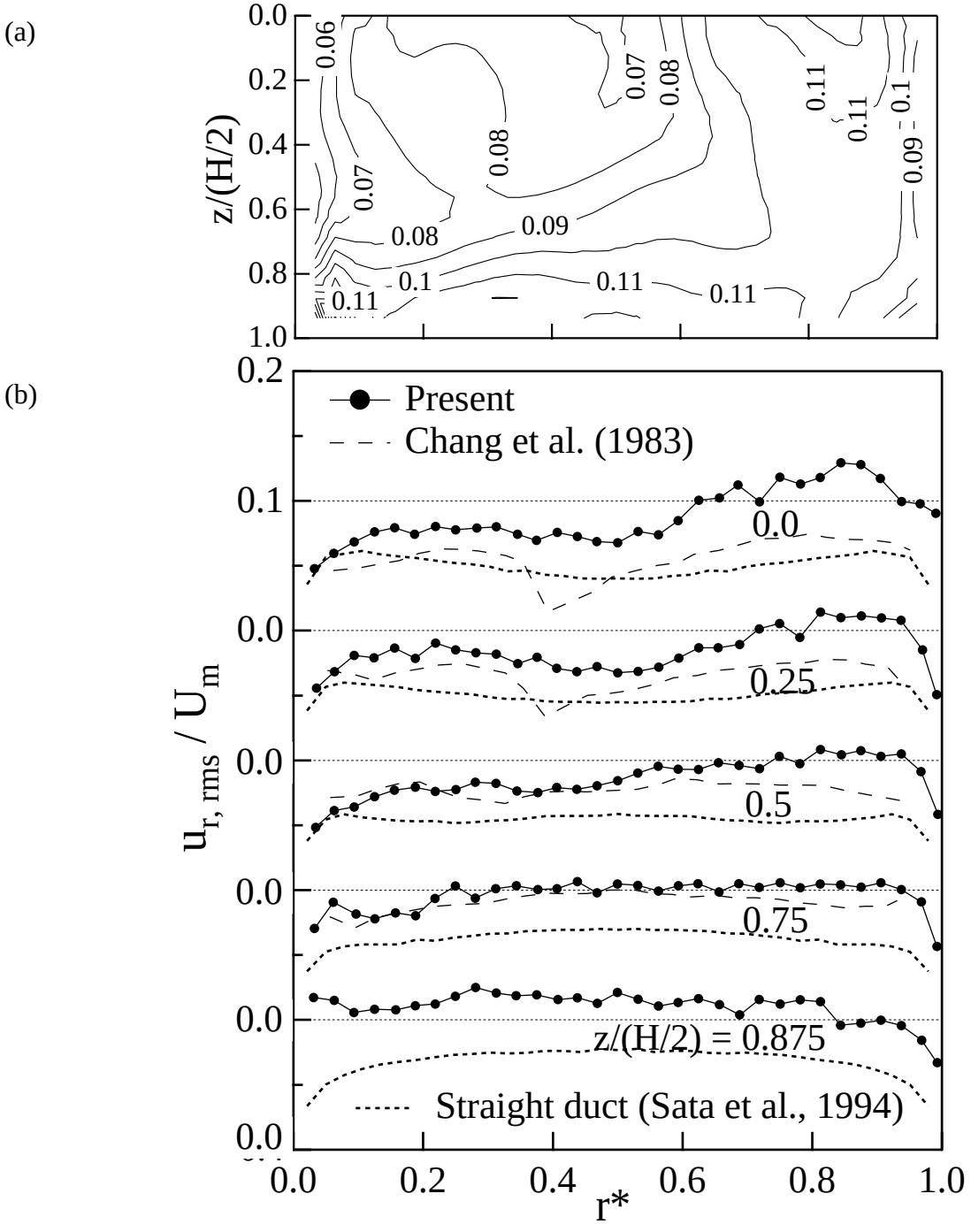

Fig. 19 Distributions of radial RMS velocity fluctuations. (a)Contours, (b)Profiles at five elevations from the bottom wall.

(a)

(b)

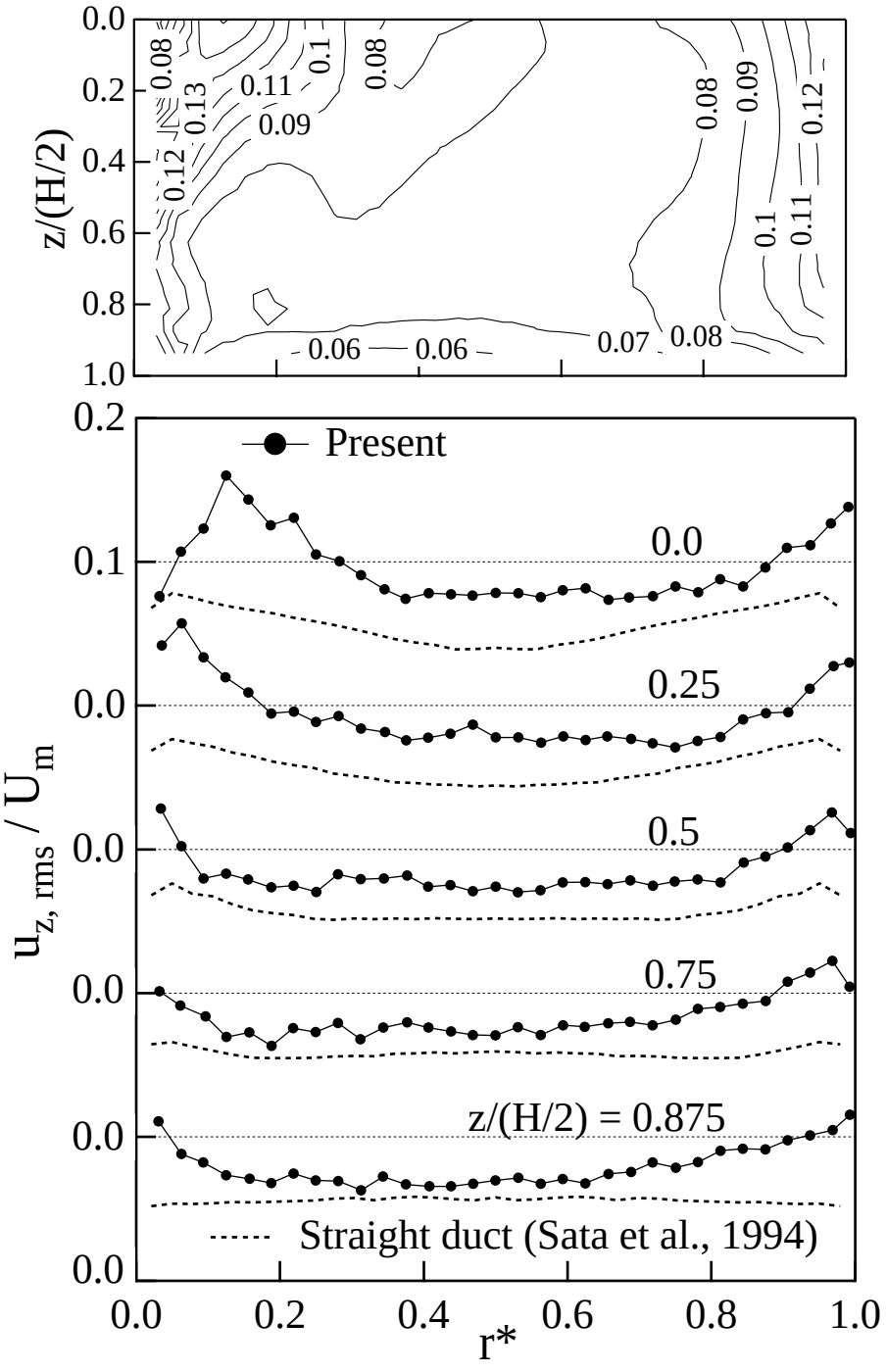

Fig. 20 Distributions of vertical RMS velocity fluctuations. (a)Contours, (b)Profiles at five elevations from the bottom wall.

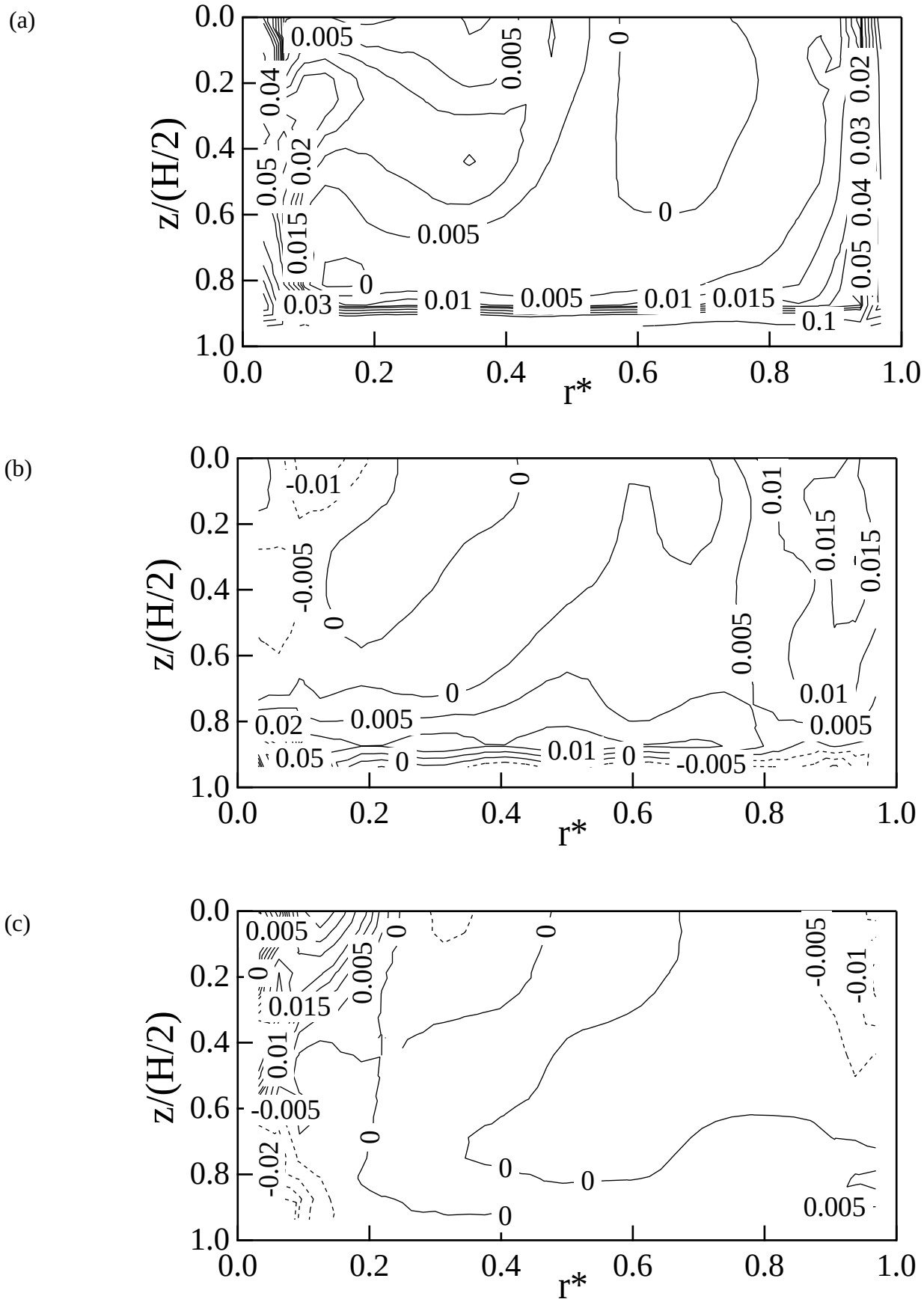

Fig. 21 Contours of the production terms in the transport equation of the Reynolds normal stresses. Broken lines denote negative contours. (a) Tangential, (b) horizontal, (c) vertical component.

(a)

(b)

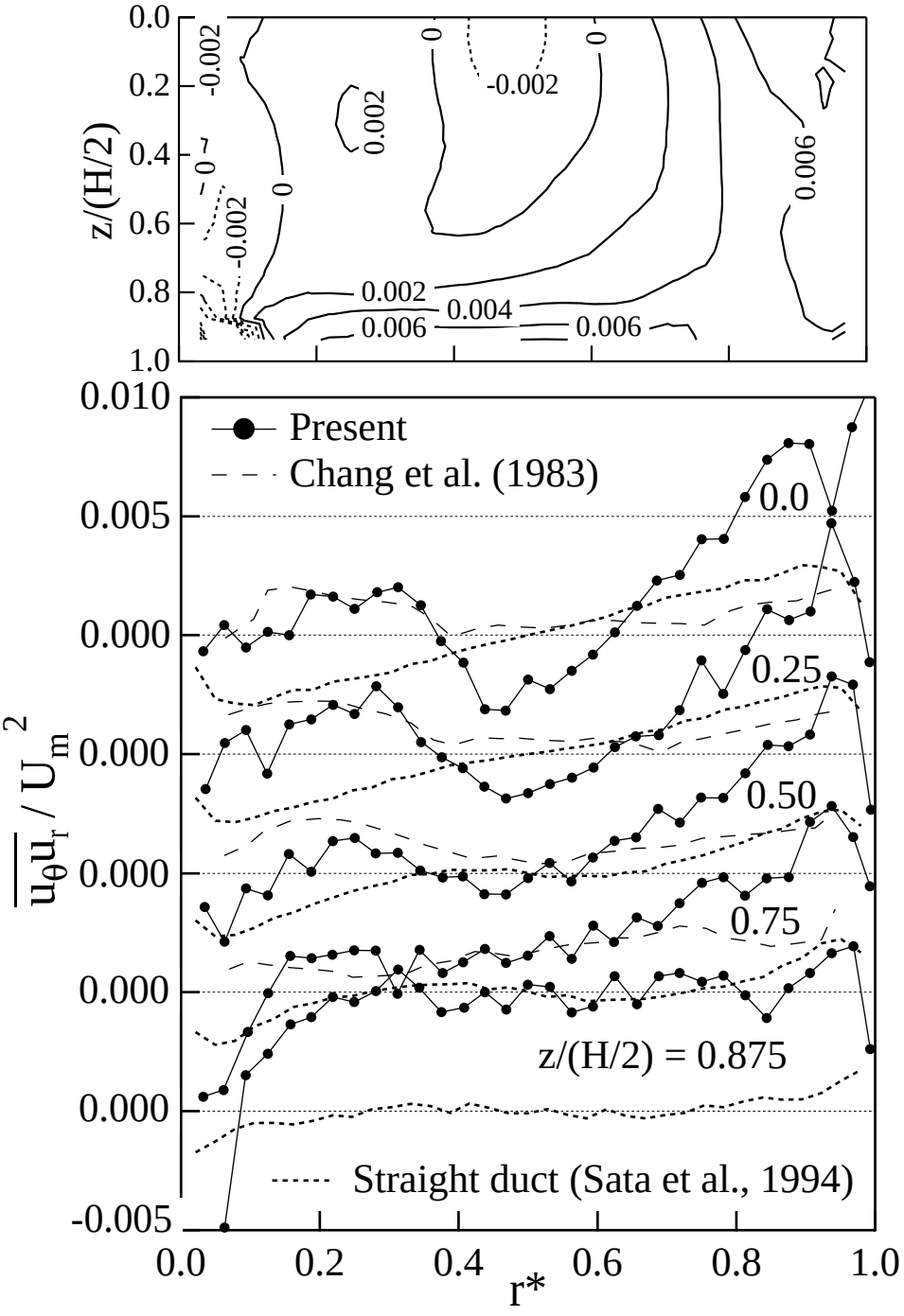

Fig. 22 Reynolds shear stress distributions. (a)Contours of $\overline{u_\theta u_r}$, (b)Profiles of $\overline{u_\theta u_r}$ at five elevations from the bottom wall (Broken lines denote experiment data $\overline{u_x u_z}$ of Sata et al. (1994) in a straight square duct), (c)Contours of $\overline{u_\theta u_z}$, (d)Contours of $\overline{u_r u_z}$.

(c)

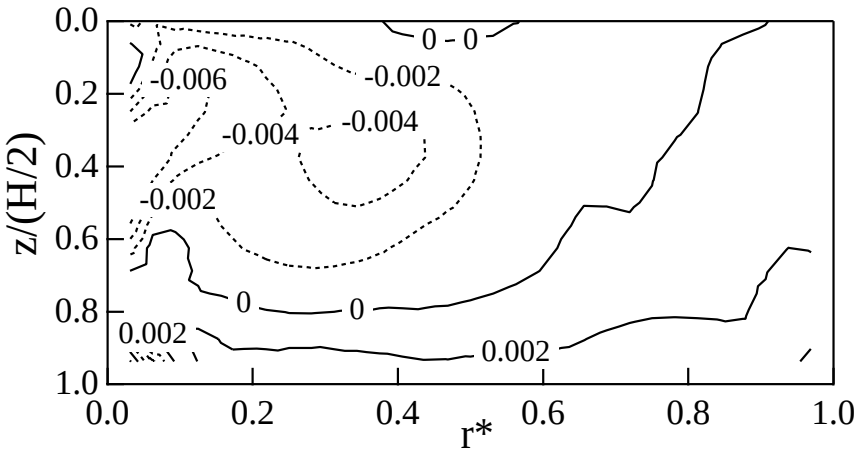
0.0
0.2
0.4
0.6
0.8
1.0
z/(H/2)
0.0
0.2
0.4
0.6
0.8
1.0
r*
0 - 0
-0.006
-0.002
-0.004
-0.004
-0.002
0
0
0.002
0.002

(d)

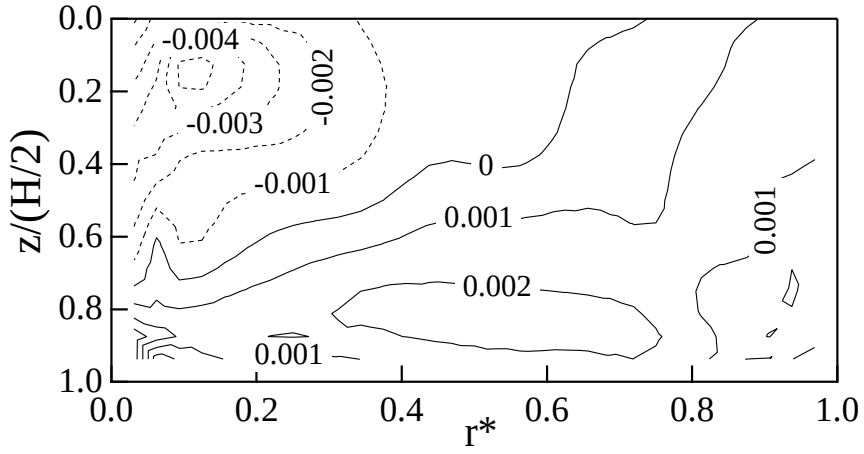
0.0
0.2
0.4
0.6
0.8
1.0
z/(H/2)
0.0
0.2
0.4
0.6
0.8
1.0
r*
-0.004
-0.002
-0.003
-0.001
0
0.001
0.001
0.002
0.001

Fig. 22 (c), (d)

(a)

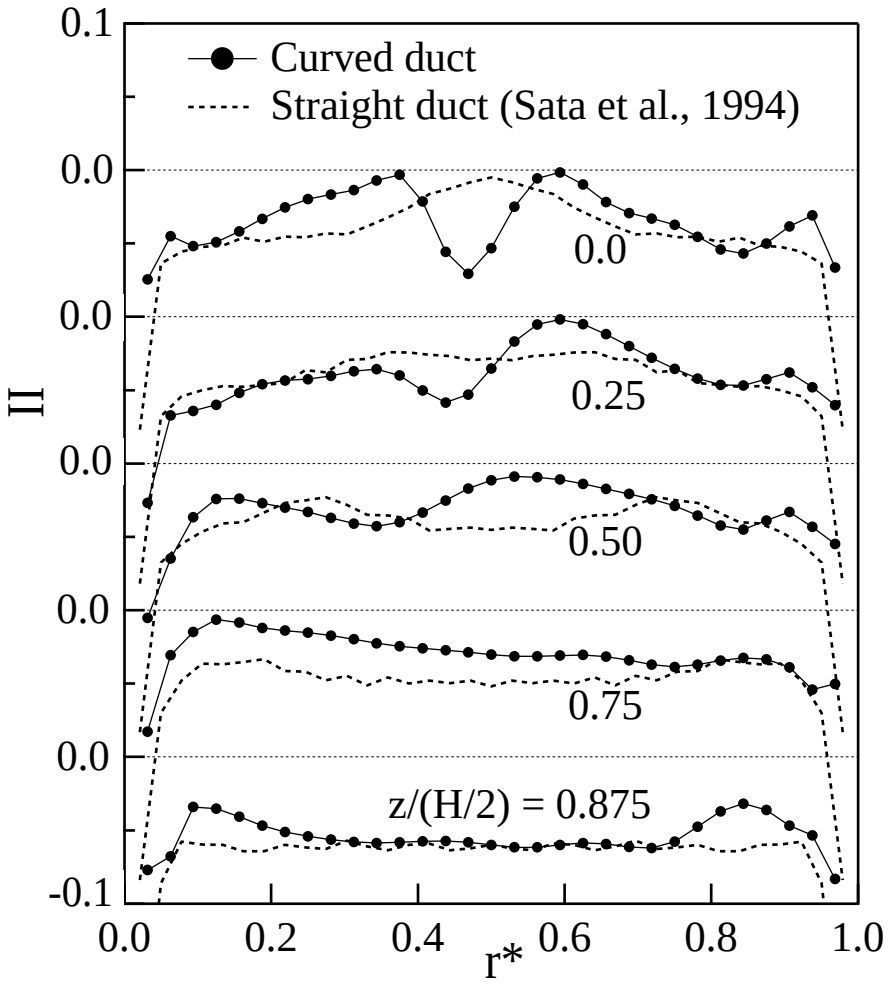

Fig. 23 Profiles of invariants of anisotropy tensor at five elevations from the bottom wall. (a) Secont invariant, (b) Third invariant.

(b)

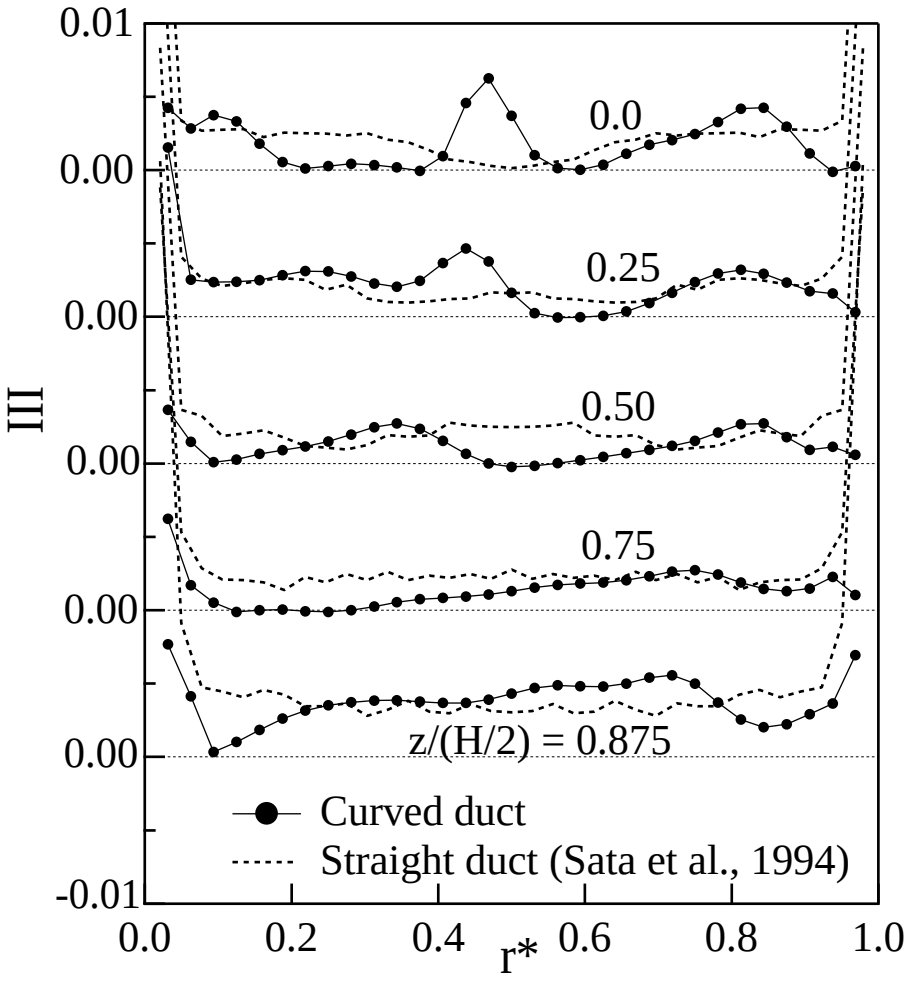
0.01
0.00
0.00
0.00
0.00
0.00
-0.01
III
0.0
0.25
0.50
0.75
z/(H/2) = 0.875
Curved duct
Straight duct (Sata et al., 1994)
0.0
0.2
0.4
0.6
0.8
1.0
r*

Fig. 23 (b)

(a)

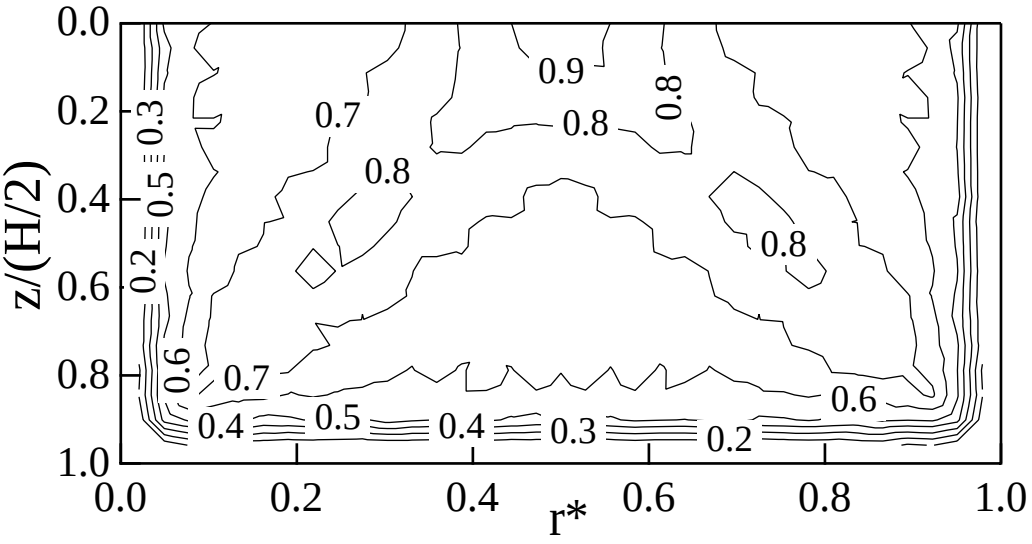

(b)

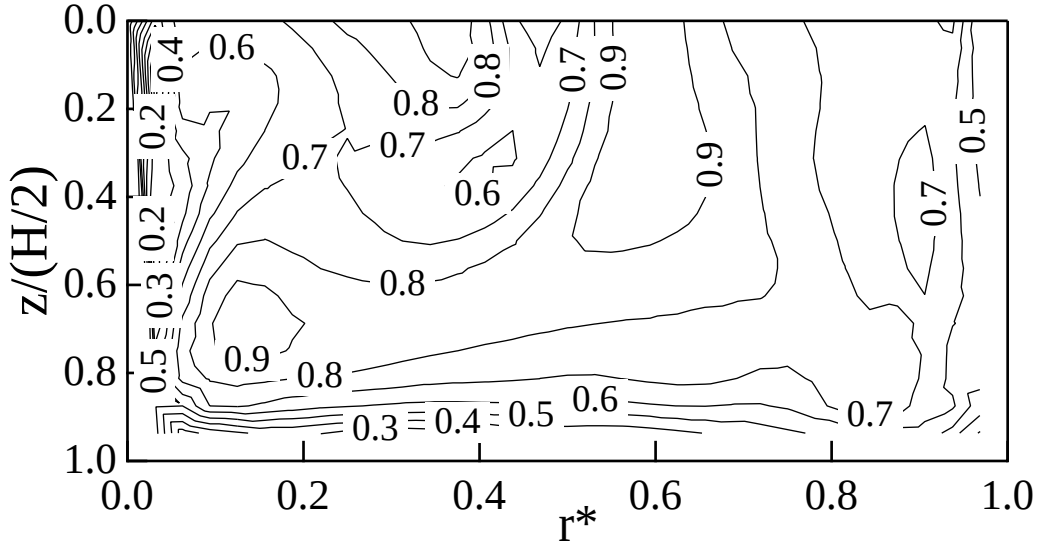

Fig.24 Contours of flatness parameter, *A*. (a) Straight duct (Sata et al., 1994), (b)Curved duct.